NASA
Technical
Paper
2571

May 1986

Rail Accelerators for Space Transportation

An Experimental Investigation

Lynnette M. Zana,
William R. Kerslake,
and John L. Sturman

NASA Technical Paper 2571

1986

Rail Accelerators for Space Transportation

An Experimental Investigation

Lynnette M. Zana,
William R. Kerslake,
and John L. Sturman

Lewis Research Center
Cleveland, Ohio

National Aeronautics
and Space Administration

Scientific and Technical Information Branch

Summary

The rail accelerator is a means of electromagnetically accelerating finite-sized particles to high velocities (kilometers per second). An experimental program was conducted at the Lewis Research Center with the objective of investigating the technical feasibility of rail accelerators for propulsion applications. Single-stage, plasma-driven rail accelerators of small (4 by 6 mm) and medium (12.5 by 12.5 mm) bores were tested at peak accelerating currents of 50 to 450 kA. Three configurations of the small-bore accelerator were designed to improve the mechanical integrity of the accelerator under impulsive loading. The medium-bore rail accelerator was designed with clear polycarbonate sidewalls to permit the visual observation of the acceleration process.

This paper presents the results of 145 rail accelerator tests. Progress has been made in understanding the physics of rail accelerator operation. Technical uncertainties do exist, however, particularly with regard to the inconsistency of the rail accelerators described herein in meeting theoretical performance expectations. The disparity between theoretical and experimental performance has been attributed to several factors, some of which may derive from the use of a plasma armature as the driving mechanism. Streak-camera photography, used with the medium-bore rail accelerator, provided a qualitative description of plasma armature acceleration and aided in the identification of an arc-ablative phenomenon which may inhibit performance. Other possible causes of poor accelerator performance, including the effects of plasma blowby and the importance of structural integrity, are discussed.

Introduction

NASA has an ongoing interest in advanced space propulsion concepts. The demand for cost effective, mission-enabling propulsion systems has greatly increased because of the commitment to a manned presence in space and the potential growth of large material delivery requirements to space.

Electromagnetic launcher concepts date back to the early 1900's but received little notable attention until 1972 when researchers at Australian National University used a 3-m-long railgun and a 500-MJ homopolar generator to accelerate a 3-g mass to 6.9 km/sec (refs. 1 and 2). The demonstration that gram-sized projectiles could be launched to high velocities prompted NASA to investigate the use of rail accelerators for larger scale space propulsion applications, including the delivery of ton-size, nonfragile payloads to space.

The NASA Lewis rail accelerator research program began in 1980 and focused on two main efforts. Mission-defining studies were conducted to evaluate the technical merit and to estimate the cost benefits of using rail accelerators for various to-space and in-space propulsion missions. A synopsis of these mission studies (refs. 3 to 5) is included in appendix A.

A parallel effort consisted of laboratory research to investigate technical feasibility issues. Initial experiments examined the performance of a single-stage rail accelerator designed for high velocities (>10 km/sec). A 3-m-long, 4- by 6-mm-bore rail accelerator was tested using a 374-kJ capacitor bank at Lawrence Livermore National Laboratory. Results of the tests are reported elsewhere (refs. 6 to 8) and will not be presented in detail here. Between 1981 and 1984, rail accelerator tests were also conducted at Lewis. Using a 5-kJ capacitor bank, very small (3-mm^2 bore) rail accelerators were tested primarily to demonstrate concept and to gain a first-hand understanding of the physics principles (ref. 9). A 240-kJ electromagnetic propulsion test facility was assembled and made operational in August 1983. By October 1984, when the program funding was discontinued, 145 rail accelerator tests had been conducted with 1-m long, small- and medium-bore rail accelerators. This report documents those test results.

The initial objective of the experimental program was to demonstrate the plasma armature acceleration of projectiles to high velocities (>10 km/sec). Energy storage limitations dictated a small accelerator bore size. In theory, using 240 kJ of stored energy, a 0.2-g mass could be accelerated to ~ 15 km/sec in 3 m with a 200-kA peak current. Therefore, it was necessary to find a small-bore structural configuration that could withstand the impulsive loading of a 200-kA peak current. The performance of each structural configuration was characterized. Three configurations of a 1-m-long, small-bore rail accelerator were designed and tested at peak currents to 230 kA. It was hoped the most successful of these could be extended to 3 m in order to reach the high-velocity objective.

Another primary objective was to understand the physics of plasma armatures over a scaling range sufficient to anticipate the performance of the meter-size bore rail accelerators required by the large-scale mission applications described in appendix A. A 1-m-long, medium-bore (12.5- by 12.5-mm) rail accelerator was designed with clear polycarbonate sidewalls to visually observe the arc/projectile dynamics during acceleration. (Larger bores, up to 100 mm^2, were envisioned for

future testing.) This design was used for a number of tests to photograph the plasma arc formation and acceleration, to measure performance as a function of accelerating current level and bore pressure, and to determine the effects of plasma blowby on performance. Unconfined plasma tests were also performed at various bore pressures.

The first portion of this paper presents the theory of rail accelerator operation and gives a brief description of the NASA Lewis 240-kJ rail accelerator test facility. Detailed descriptions of the small- and medium-bore rail accelerators are given along with design considerations. Diagnostic techniques to obtain information on plasma arc/projectile acceleration in-bore as well as the electrical characteristics of the rail accelerator and system is also discussed.

The major portion of this paper presents the results of 145 tests with the small- and medium-bore rail accelerators. Performance trends for all accelerator designs are discussed. Representative tests are explained in detail; however, the bulk of data are presented in tabular form and in figures. Streak-camera photographs of selected tests are also presented.

This paper also describes a photonic sensor technique to measure bore pressure during a rail accelerator test. Also, the use of a high-current ignitron (closing switch) in crowbar service in the pulsed power system is described. The resistance characteristics of the ignitron and their impact on pulse shaping is discussed.

Symbols

A_o bore area, m^2

A_u unsealed bore area, m^2

a acceleration, m/sec^2

B magnetic field, T

C total circuit capacitance, F

E electric field, V/m

E_0 energy store in banks, $\frac{1}{2} CV_f^2$

F Lorentz force, N

I total current, A

I_L load current, A

I_{pk} peak current, A

J current density, A/m^2

L total inductance, H

L' inductance gradient, H/m

L'_{av} average, instantaneous L', H/m

L'_{eff} effective inductance gradient, H/m

L_{sys} system inductance, H/M

m mass, kg

P_T tank pressure (assume equal to bore pressure in front of projectile), MPa (torr)

R total resistance, ohm

R_{sys} system resistance, ohm

t time, sec

t_c time when capacitor bank crowbarred, sec

t_f time when projectile exits muzzle, sec

t_{pk} time to peak current, sec

V_b bank voltage when fired, V

V_c bank voltage at charge, V

v projectile velocity, m/sec

v_f final projectile velocity, m/sec

$v_{1\text{-}2}$ velocity as measured by velocity stage 100 cm downstream of muzzle, m/sec

x distance along accelerator length (x = 0 at breech), m

y transverse distance, m

Subscripts:

a arc

e electron

i ion

p projectile

r rail

Physics of Rail Accelerator Operation

The basic rail accelerator configuration (fig. 1) consists of two long, parallel conductors (rails) bounding an electrically insulated projectile. A conductive armature, whether solid or plasma, is placed behind the projectile. Current flowing through one rail, across the armature, and returning through the other rail generates a magnetic field. The interaction of the current with the field between the rails produces a Lorentz force ($J \times B$) which accelerates the armature. The projectile, then, can be accelerated with a force that is proportional to the current squared. Specifically,

$$F = \frac{1}{2} L' I^2 \tag{1}$$

where L' is the inductance per unit length of the accelerator and I is the current. High acceleration requires an accelerator design with a high L' matched to a high current energy source.

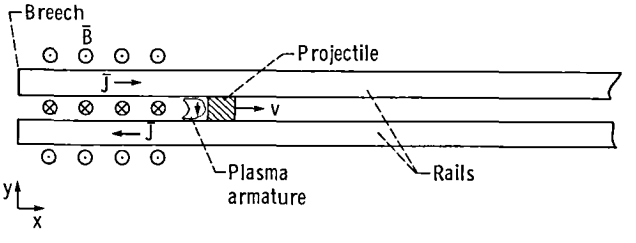

Figure 1.—Basic rail accelerator configuration. Distance along accelerator length, $x=0$ at breech.

Typical rail accelerator operation involves currents on the order of 10^5 to 10^6 A with acceleration times of only a few milliseconds. One method of operating a rail accelerator uses energy storage capacitors matched to a low-impedance inductor as the power source. A simplified electrical schematic for the tests described herein is shown in figure 2. The capacitive energy is discharged via firing switch S_1 through the inductor, L_{sys}, to the rail accelerator. When the capacitor bank has fully discharged, that is, when bank voltage is zero, crowbar switch S_2 is closed (S_1 open) to prevent high current and voltage reversals. The resultant current pulse is determined by the electrical characteristics of the system (L_{sys} and R_{sys}) and the accelerator load. Electrically, the rail accelerator may be represented as a variable inductance and resistance load. It is an inherently inefficient device in that only a fraction of the energy supplied to the accelerator is converted into the kinetic energy of the projectile. This inefficiency is due to the high resistive heating losses in the rails and armature and to the energy which remains stored in the magnetic field between the rails. Efficiency rises with higher projectile velocity but is limited in a single-stage rail accelerator. Extremely long accelerators can have excessive resistive losses. High acceleration is also dependent on the inductance gradient L'. For uniform current density in the rails (dc case), the inductance gradient is dependent solely on the geometry of the rails and can be calculated easily (ref. 10). Typical L' values are 0.5 to 0.6 μH/m in the direct current limit. However, because of electrical skin effects in high-frequency pulsed-power operation, the current density is not uniformly distributed over the rail cross section as it would be in the direct-current case. Consequently, the L' available for ideal Lorentz acceleration becomes smaller and is a transient parameter dependent on current diffusion to the center of the rails (refs. 11 and 12). It typically lies between the values for the direct-current and high-frequency limit cases. The high-frequency limit (HFL) case assumes that the current is confined to a thin outer sheath of the rail.

Use of a Plasma Armature

A plasma armature was chosen as the driving mechanism for the projectile because it has low mass, makes good electrical contact with the rails, and has adequate electrical conductivity. The plasma armature may be initiated with a thin piece of aluminum foil attached to the backface of the projectile. When the rail accelerator is fired, the high current passing through the foil vaporizes it and forms a plasma. The plasma remains confined by the induced magnetic field and the projectile in front of it.

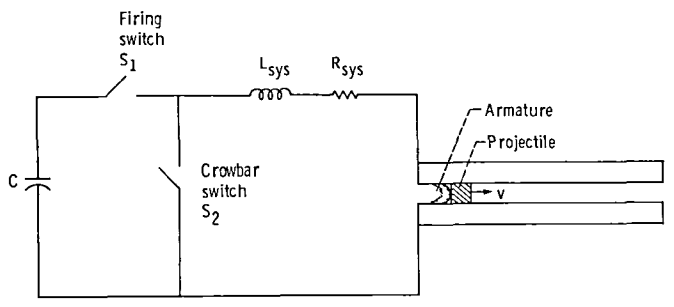

Figure 2.—Simplified electrical schematic of pulsed power system.

Theoretical groundwork in the characterization of the plasma armature was done by McNab (ref. 13). Powell and Batteh extended (ref. 14) this model with a detailed fluid mechanical and electrodynamic analysis. Assuming a steady-state solution, major flow variables such as pressure, electron number density, and temperature were found to vary nonlinearly with position in the arc. Powell (ref. 15) later extended the model to two dimensions. A computer simulation code developed by Thio (ref. 16) models and predicts the physical properties of a quasistatic plasma armature.

A simplified analysis has been put forth by Ray (ref. 17). As stated previously, the projectile is accelerated by the pressure of the confined plasma behind it. The plasma is assumed to be fully ionized. Current flowing through the plasma sets up an electric field between the two conducting rails (fig. 3). One rail acts as a cathode (−), and the other as an anode (+). The electrons and ions in the plasma acquire drift velocities denoted by v_e and v_i, respectively ($v_e \gg v_i$). The flow of current in the plasma also induces a self-generated magnetic field B. The Lorentz forces produced by the interaction of the current in the plasma and the field between the rails cause the electrons and ions to accelerate in the x-direction. The electrons experience higher acceleration than the ions because they have a much smaller mass. Consequently, charge separation occurs at the plasma boundaries. The electrons attach themselves to the rear of the projectile (typically a dielectric) with the ions at the opposite boundary. The main body of the plasma remains electrically neutral.

To oppose this separation of charges, an electric field (Hall field), E_x, is also set up in the plasma; charge separation ceases when this electric force balances the Lorentz force on the electrons. The ions now experience a net force in the x-direction and begin to accelerate. The electrons, attached to the base of the projectile, also accelerate to maintain charge separation. The plasma and projectile, then, accelerate together. It is apparent that a tight bore seal between the projectile and sidewall surfaces is necessary to prevent the low mass plasma from accelerating past the projectile (plasma blowby).

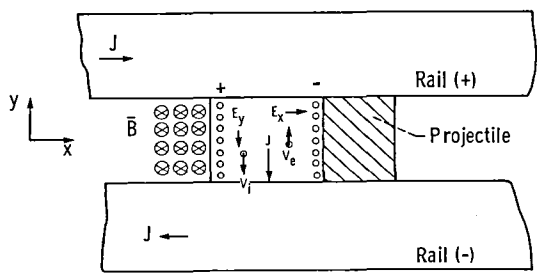

Figure 3.—Mechanism of plasma armature acceleration. Magnetic field induced by current density J causes separation to occur at plasma boundary. The main body of the plasma remains electrically neutral.

Rail Accelerator Performance

Equation (1) can be rewritten in terms of acceleration and integrated to give an equation for final projectile velocity:

$$v_f = \frac{L'}{2m}\int_0^{t_f} I^2(t)\,dt \tag{2}$$

The integral in equation (2) is defined as action and reflects the total impulse input to the accelerator until the time t_f that the projectile leaves the muzzle.

Since m, v_f, t_f, and $I(t)$ are all measured quantities, overall rail accelerator performance can be quantified with the use of an effective inductance gradient, L'_{eff}. Rearranging equation (2) gives

$$L'_{\text{eff}} = \frac{2mv_f}{\int_0^{t_f} I^2(t)\,dt} \tag{3}$$

The effective inductance gradient serves as a measure of the actual accelerating force (less any force losses) imparted to the projectile. It can be compared with the ideal inductance gradient L' for Lorentz acceleration and provides a quantitative measure of the correspondence between the experimental accelerator performance and the theoretical expectations. It is the primary means of evaluating rail accelerator performance used in this report.

Apparatus

Rail Accelerator Test Facility

The rail accelerators tested at NASA Lewis used pulses of 50- to 450-kA peak current with pulse lengths of up to 1 msec. Energy storage capacitors matched to a low-impedance inductor served as the power source. (See fig. 2.) Total circuit capacitance was varied from 1.26 to 5.06 mF at voltages up to 10 kV. System inductance was typically 1.7 μH, but a large storage coil (12.2 μH) could be added to the circuit to provide longer pulse lengths.

Figure 4 displays a layout of the 240-kJ test facility. Energy storage is provided by four 60-kJ capacitor bank modules. Each module consists of six 200-μF, 10-kV capacitors equipped with individual feed-forward ignitrons (firing switches). A large, single-ignitron (crowbar switch) placed across each module isolates the bank from the load circuit once it has discharged. The output of each module is connected to a common distribution header and then is fed coaxially into a vacuum test chamber. The test chamber can accommodate rail accelerators up to 6 m long and can be operated at tank pressures from 0.5 to 100 kPa (4 to 750 torr).

The capacitor bank modules are charged from a single direct-current power supply located in the control console. The 10-kV, 2-A supply can fully charge the system in less than 60 sec. The discharge of the bank (the triggering of the firing and crowbar switches) is also controlled by the console which is located in a room adjacent to the test facility. All major elec-

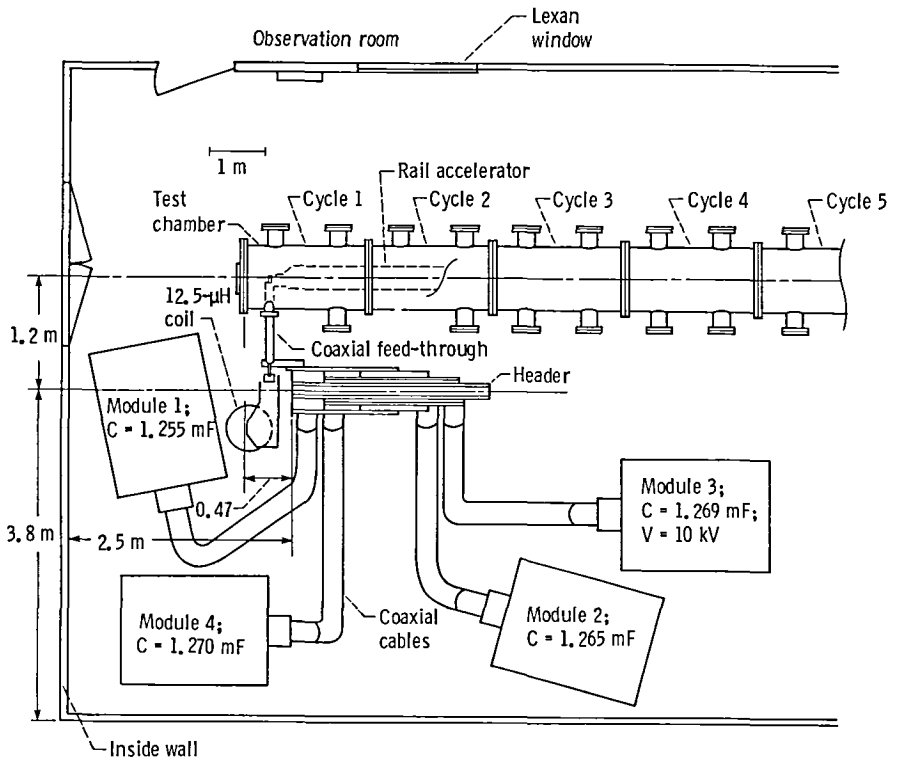

Figure 4.—240-kJ Rail accelerator test facility.

tronics (oscilloscopes, etc.) are housed in this room. Complete details of the design, installation, and operating characteristics of this facility are found in reference 18.

Rail Accelerator Test Designs

One-meter-long, small-bore rail accelerators.—As stated previously, high acceleration requires an effective rail accelerator design (high L') matched to a high current energy source. To reach the 10- to 15-km/sec velocity goal, the size of the available energy store dictated a small projectile mass (0.2 g) and, therefore, a small-bore configuration (4 by 6 mm). The necessary rail accelerator length was 3 m, and the accelerating stress on the projectile was 400 MPa (peak current, 200 kA). The desire to maximize L' defined the rail size and bore geometry.

Launcher stress poses a serious problem in design considerations. Under impulsive loading, magnetic repulsion forces the rails outward, imposing severe stresses on the accelerator structure. These outward rail forces may be as high as 10^4 to 10^5 N. An early test series conducted at Lawrence Livermore (refs. 6 to 8) with a 3-m-long, 4- by 6-mm bore rail accelerator exposed the problem. The 3-m-long accelerator structure (design A) failed materially after repeated firings at a 110- to 140-kA peak current.

Three configurations of a 4- by 6-mm bore rail accelerator were designed and tested at Lewis. The objective was to find a configuration that could maintain structural integrity (tight bore seal and no material failure) under the stress load due to peak currents up to 200 kA and give nominal performance. The three accelerators were tested in 1-m-long sections to evaluate performance and to determine necessary design guidelines. It was hoped that one design would later be extended to 3 m to reach the high velocity objective.

Figure 5 displays the first of the three small-bore designs tested (design B). The accelerator bore was defined by two 6-mm^2, half-hard copper rails held in place by two pieces of G–10 insulation. The rails were machined to a 0.02-mm tolerance. The G–10 insulation is a laminated plastic consisting of a reinforced fiberglass base material with an epoxy resin. It was chosen as the insulation material because of its combination of good electrical, thermal, and mechanical properties. The mechanical strength properties of G–10 in the planes perpendicular to the fiber layers are excellent (tensile strength, 276 to 310 MPa; compressive strength, 414 MPa). However, the parallel-to-fiber layer direction has very poor mechanical strength properties. The accelerator design was configured so that the outward rail forces would work against the strongest G–10 properties. The inner G–10 structure pieces were round-fit to an outer structure also made of G–10. The plane of the rails was oriented in a direction perpendicular to the outer structure fiber layers. Phenolic backing plates (3.75-cm thick) and high-strength stainless-steel bolts clamped the entire structure together. The clamping action was against the outward rail forces. The clamp design was chosen for ease of assembly. The design minimized metallic components near the bore to keep L' as high as possible. This accelerator design was extended to 3 m for two tests. Figure 5(b) shows a supporting cart used to roll the heavy assembly into the test chamber.

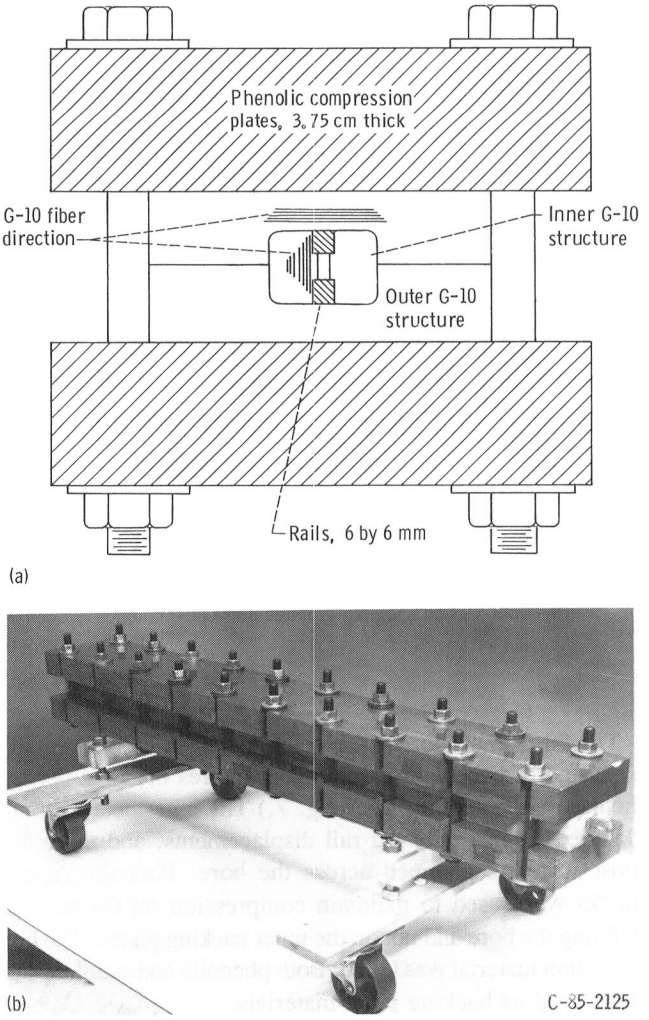

(a) Cross section of accelerator structure.
(b) Assembled structure.

Figure 5.—1-m-long, 4- by 6-mm-bore, design B rail accelerator.

The second small-bore rail accelerator design investigated the novel use of composite insulation (fig. 6). The bore was defined by two 6-mm^2 rails and two inner structure pieces of G–10 insulation. In this design the outer structure was machined from a reinforced-fiberglass, filament-wound composite tube. The laminations ran in nearly circular fashion around the inner structure and were always perpendicular to outward forces. One accelerator of this design had an all fiberglass (G–10) outer structure. A second had a composite outer structure consisting of graphite and fiberglass. The major portion of the outer structure was graphite, with 6.4-mm-thick layers of G–10 insulation at the inner and outer surfaces. Figure 6(b) displays two halves of the graphite/G–10 composite tube. The structure pieces were faced off, top and bottom, to provide a flat clamping surface. They were also shaved minimally at the sides to provide a close fit between clamping bolts.

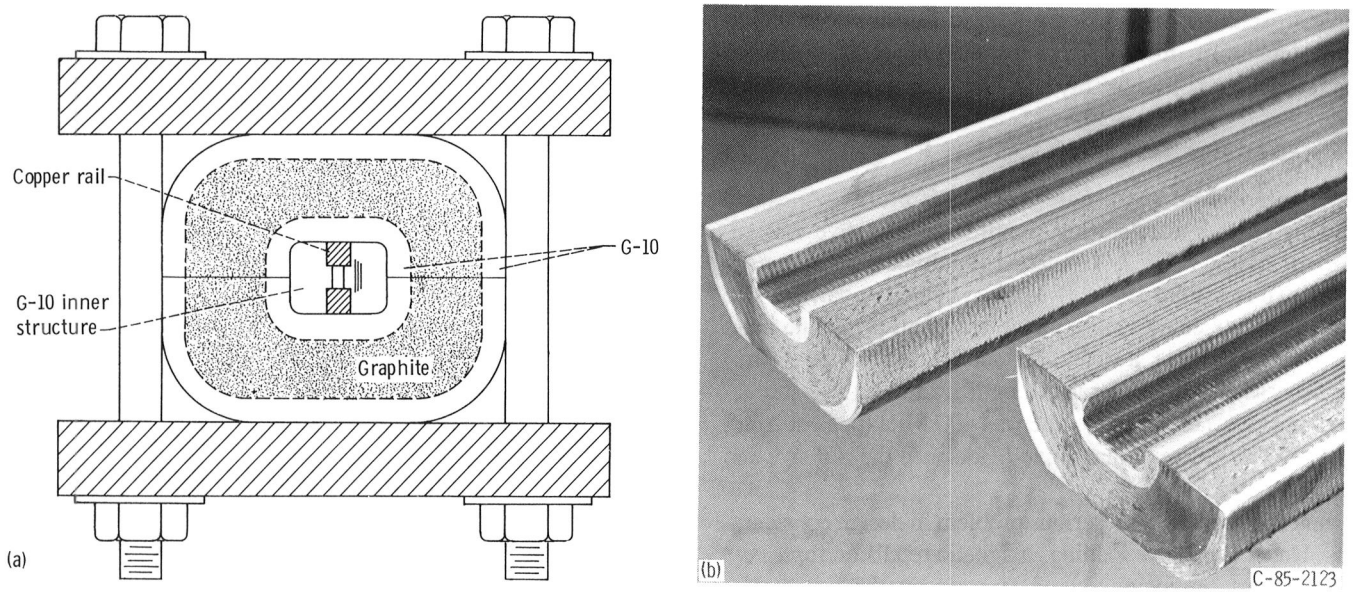

(a) Cross section showing graphite and G–10 composite outer structure. Note that laminations run in nearly circular fashion around bore.
(b) Filament wound outer structure pieces.

Figure 6.—1-m-long, 4- by 6-mm-bore, design D, rail accelerator.

The third small-bore rail accelerator (design D) essentially consisted of two outer clamping structures oriented perpendicular to one another. (See fig. 7.) The innermost structure clamped against outward rail displacements, and the outermost structure clamped across the bore. Phenolic support blocks were used to maintain compression on the surfaces defining the bore and not on the inner backing plates. The bore insulation material was G–10. Both phenolic and stainless steel were used as backing plate materials.

Despite apparent outer structural differences, the rail size and bore geometry for each of the above designs were the same. The geometric inductance gradient L' for this rail configuration was calculated at 0.60 μH/m for the direct-current case (ref. 10) and 0.46 μH/m for the high-frequency limit case (ref. 11). Inductance bridge measurements confirmed the calculated value in the direct-current case: 0.49 μH/m was measured in the HFL case. As mentioned previously, the actual value of L' available for ideal Lorentz acceleration lies between the two limiting values. A simple model for current diffusion can be used to approximate an average value of L' for the duration of a typical pulse length. Instantaneous L' values can be calculated at discrete time intervals and then

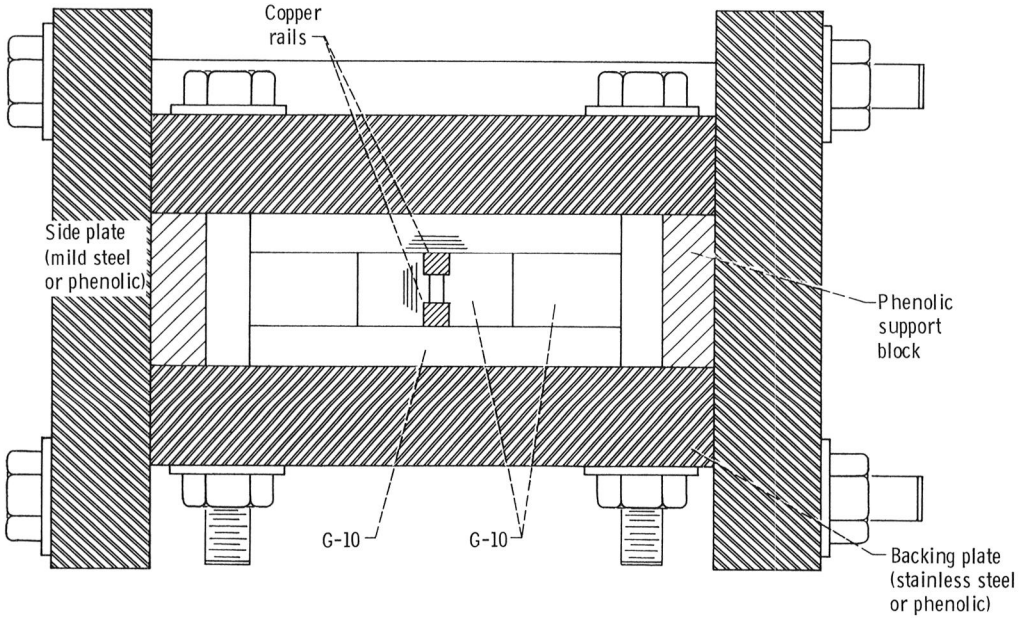

Figure 7.—1-m-long, 4- by 6-mm-bore, design D, rail accelerator; double squeeze assembly.

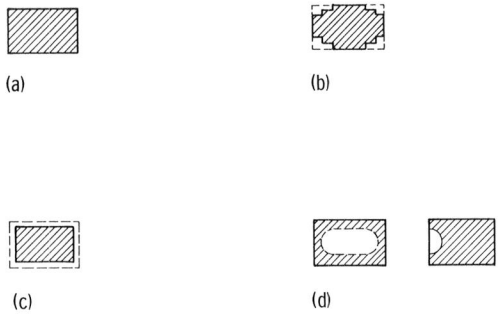

(a) Standard projectile.
(b) Grooved projectile.
(c) Undersized projectile.
(d) Projectile scooped out at rear face of projectile.

Figure 8.—Cross sectional views of projectiles tested in the small-bore rail accelerators.

averaged over the duration of acceleration. For a typical current pulse of 200 kA, an average, instantaneous value, L'_{av}, for the small-bore configuration has been calculated at 0.52 μH/m (authors'calculations).

Figure 8 displays the various types of projectiles tested with the small-bore rail accelerators. Unless otherwise specified, the standard projectile was a rectangular polycarbonate block (Lexan), machined to dimensions 0.02 mm smaller than the bore size (fig. 8(a)). Special tests required slight design modifications as detailed in figures 8(b) to (d). The grooved and undersized projectiles (figs. 8(b) and (c)) were tested with the objective of examining the effects of an unsealed bore on performance. The intention of the scooped back design (fig. 8(d)) was to produce a tighter bore seal between the projectile and sidewalls. The plasma pressure on the backface of the projectile would, in theory, force uniform expansion of the plastic projectile material, creating a tighter seal. The 4- by 6-mm projectiles typically weighed 0.16 to 0.20 g. The usual projectile starting position was 2.54 cm from the breech of the rail accelerator. The plasma armature was initiated with a 0.025-mm thick piece of aluminum foil.

One-meter-long, medium-bore rail accelerator.—The medium-bore (12.5 by 12.5 mm) rail accelerator (fig. 9) was designed to permit visual observation of plasma armature acceleration. The rails were 12.5- by 18.5-mm copper bars, machined to a 0.02-mm tolerance. They were seated in a cross-shaped bore structure piece such that they defined a 12.5 mm^2 bore. The bore structure piece, a high-strength, clear polycarbonate (Lexguard), provided an uninterrupted view of the entire accelerator. The outer structure material was of G–10. Stainless-steel bolts (4.8 mm diam) were added at 2.5-cm intervals to provide added strength against shear forces and tension. The clamping action of the phenolic backing plates was against the outward rail forces. The copper and G–11 breech clamp assembly at the right end of the structure (fig. 9(b)) connected the rail accelerator both mechanically and electrically to the coaxial feed-through in the test chamber. The geometric L' of this bore configuration was 0.52 μH/m (dc case; ref. 10), and 0.38 μH/m (HFL case; ref. 11). The

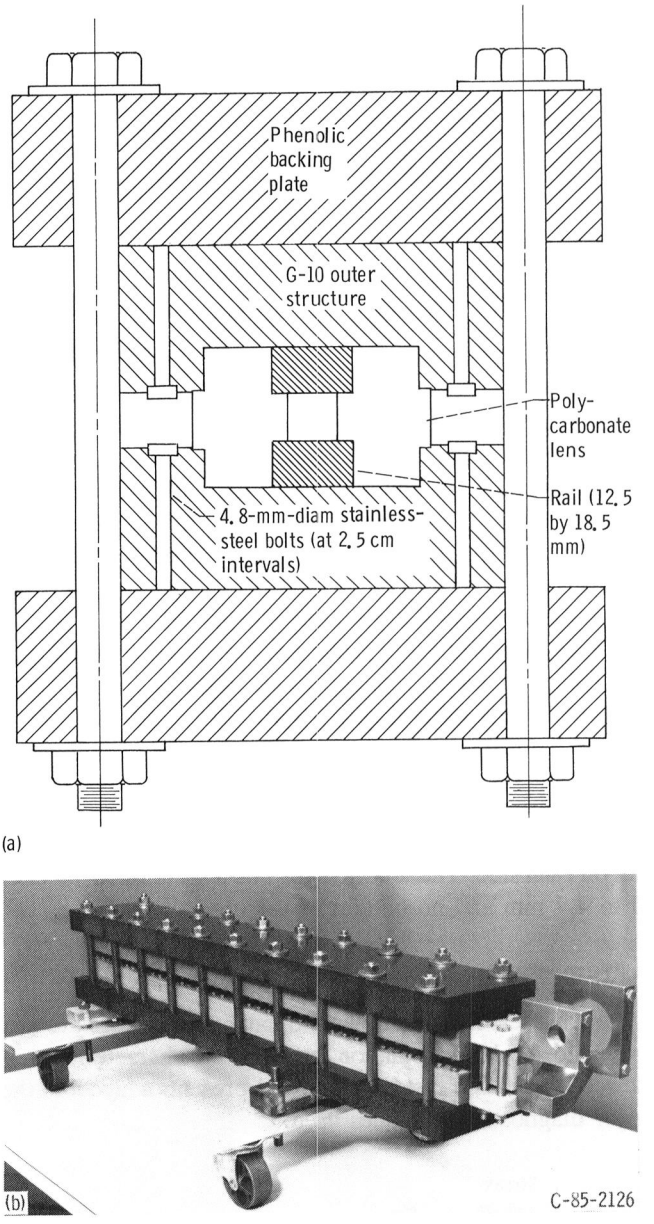

(a) Accelerator cross section. Note: G–10 may be used in place of polycarbonate lens piece.
(b) Assembled accelerator with Lexguard Sidewalls.

Figure 9.—1-m-long, medium-bore rail accelerator.

calculated average, instantaneous value was 0.43 μH/m (authors' calculations).

Figure 10 shows the projectiles for the medium-bore rail accelerator. The standard projectile was a clear polycarbonate cube of approximately 12.5 mm^2 cross section, hand-fit to the bore dimensions (fig. 10(a)). It had a 9.09-mm-diameter hole drilled into its front to a point 3.2 mm from the rear. This hole reduced projectile mass to achieve greater velocity and moved the center of mass to the rear of the projectile to help prevent in-bore chattering (communcation with K.A. Jamison of Ballistic Research Laboratory). A 1.6-mm-thick piece of black rubber served as a seal (obturator) at the backface of

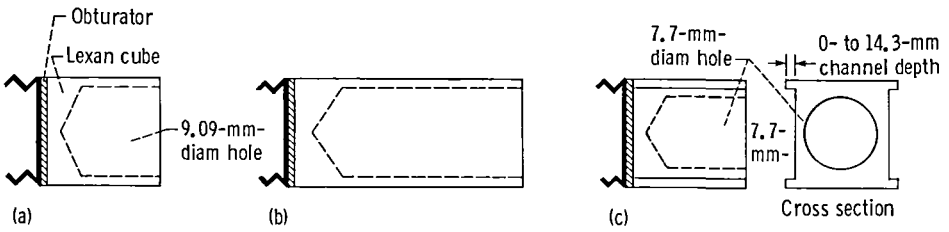

(a) Standard projectile.
(b) Double-length projectile.
(c) Intentional blowby series projectile.

Figure 10.—Projectiles tested in medium-bore rail accelerator (side views).

the projectile. The usual projectile starting position was 10 cm from the accelerator breech unless otherwise noted. The plasma armature was initiated with a piece of 0.11-mm-thick aluminum foil. The ends of the foil were flapped so that the foil shorted across the rails, providing a low-impedance circuit path during charge of the banks (2-A current). The bore area at the accelerator breech was plugged with a G–10 cube to take advantage of gas dynamic pressure during foil vaporization and to aid initial projectile acceleration. A double-length projectile was also used (fig. 10(b)).

A special test series was conducted with the medium-bore rail accelerator in which plasma blowby was intentionally promoted by cutting channels of various depths into the sides of the projectiles (fig. 10(c)). The depth varied from 0 to 1.43 mm on each side. The hole size for this test series was reduced to 7.7 mm and no obturator was used.

Instrumentation

For each test firing data were obtained on in-bore arc and projectile acceleration and on the electrical characteristics of the accelerator and system. Figure 11 presents a layout of the major diagnostic techniques used.

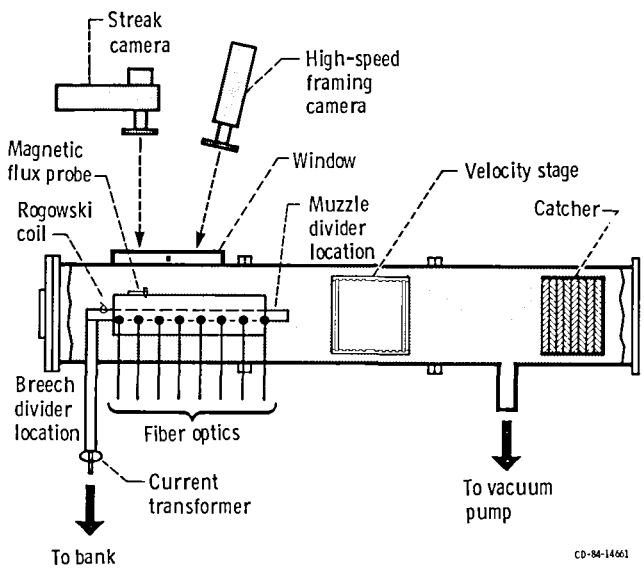

Figure 11.—Diagnostic equipment for 1-m-long rail accelerators.

In-bore arc-position data were obtained by three techniques. A set of magnetic flux (dB/dt) probes stationed at regular intervals along the length of the accelerator was used to establish the position of the arc centroid as a function of time. Each probe was a magnetic flux coil consisting of five wire turns wound on a nonmetallic rod. The axis of the probe lay parallel to the accelerator bore such that it detected only the field associated with the plasma arc. The probe produced a voltage proportional to the time rate of change of the magnetic field (dB/dt). As the arc (and projectile) approached the probe station, the magnetic field increased, reaching a maximum when the arc was directly in line with the station. Consequently, the flux through the coil also increased. The direction of the flux reversed once the arc had passed the station (B decreasing). Zero crossings on the probe voltage, then, indicated when the arc centroid was in line with the station (refs. 6 and 19).

The second in-bore diagnostic technique consisted of a set of fiber optic probes embedded with epoxy in one inner structure piece of the accelerator and coupled to phototransistors. The probes, located every 20 cm along the accelerator, responded to the luminous arc wavefront. The optical signal produced was converted to a voltage that was proportional to the luminosity.

The third technique for obtaining in-bore test data is the direct photography of the plasma armature through the Lexguard sidewalls of the medium-bore rail accelerator.

A time-of-flight device (velocity stage) was used to obtain projectile velocity during free-flight. The device consisted of two screens electrically connected to a voltage box and an oscilloscope. Each screen was made up of two isolated foil sheets separated by a piece of insulation. A battery maintained a potential drop of 450 V across the foil sheets. When the projectile pierced the first screen, the foil edges were bent from the leading foil through the insulator, so that they touched the backing foil. Thus, the battery circuit was shorted, and a pulse was sent to the oscilloscope. The projectile then pierced the second screen, sending another pulse. The time-of-flight interval between the two pulses gave the projectile velocity. The velocity stage was located approximately 1 m downstream of the accelerator muzzle. The projectile was caught in a stack of ceiling tiles (fig. 11).

A Pearson current transformer (model 2093) and a Rogowski coil were used to record the system and rail currents, respec-

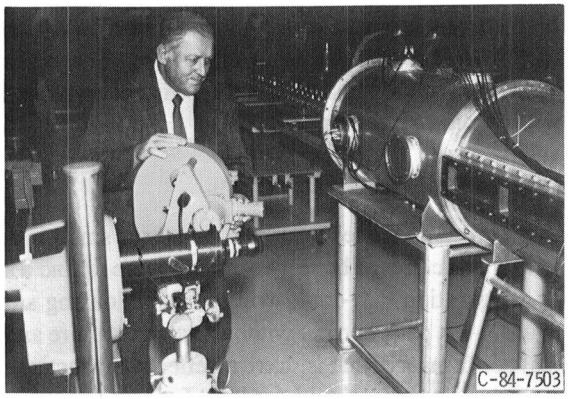

Figure 12.—Setup for streak- and framing-camera photography.

tively. Low-inductance, high-resistance ($R \approx 10$ kΩ) divider networks were used to measure the breech and arc voltages. The divider networks were magnetically shielded with Conetic metal.

During a rail accelerator test, all voltages, currents, and position data were recorded with oscilloscopes and synchronized scope cameras. The oscilloscopes were triggered by the electronic console 100 μsec before discharge of the capacitor banks.

Streak and Framing Camera Photography

High-speed photography has been used previously (ref. 20) on a small-bore (6 by 8 mm) rail accelerator. The clear Lexguard sidewalls on the medium-bore (12.5- by 12.5-mm) accelerator permitted the use of high-speed framing and streak-camera photography. A rectangular port in the wall of the test chamber allows viewing of 80 percent of the entire length of the accelerator structure. Figure 12 displays the experimental setup.

The high-speed framing camera (Fastax) provides discrete photographs of the plasma armature acceleration process. It views a section of the accelerator from a position 5 cm from the breech to approximately 75 cm downstream. The camera operates with 16-mm, half-frame film and photographs at a rate of approximately 18 000 pictures per second (every 55 μsec). A rotating prism and a 0.076-mm light limiting slit give an exposure time of approximately 1 μsec. Minor corrections for parallax were made in the final analysis.

The streak camera, on the other hand, gives an integrated view of the acceleration process. Camera operation is detailed in figure 13. Again, the camera looks at an uninterrupted section of the bore length from the breech to 80 cm downstream. Within the camera, a single 35-mm filmstrip rotates on a 27-cm drum at a rate of approximately 130 revolutions per second (rps). By means of relay lenses and a stationary relay mirror, however, the filmstrip moves in a direction perpendicular to the bore axis, that is, the arc motion, as shown by the arrows in figure 13. As the arc travels down the bore, it paints a diagonal streak across the film. The dark lines on the filmstrip mark accelerator bolt locations and serve as a convenient length scale. The slope of the streak gives wavefront velocity. Time

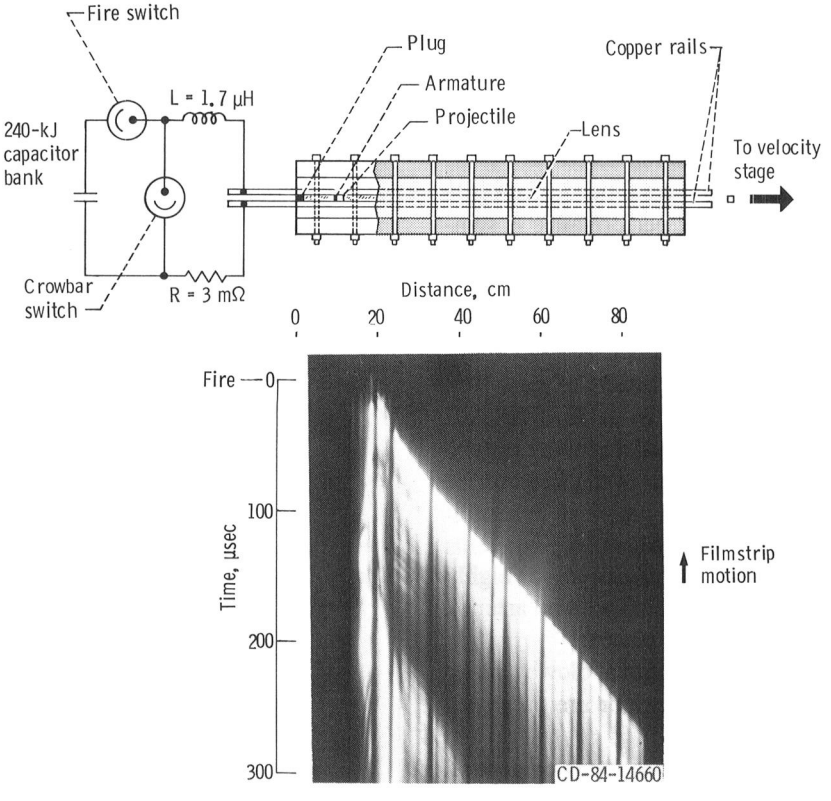

Figure 13.—Details of streak-camera operation. Note: The filmstrip moves in a direction perpendicular to arc motion.

resolution to 0.4 μsec may be obtained at writing speeds up to 0.13 mm/μsec.

Procedure

Each rail accelerator test followed an operating procedure checklist included in the actual test record. The checklist governed all aspects of the test procedure, including: pretest system checks, hardware assembly, instrumentation, pulsed-power system operation, and safety procedures.

Rail accelerators were completely refurbished between tests. The G-10 structure pieces were sandblasted and wiped clean with alcohol. New copper rail surfaces were used for each test. (Each set of rails was actually used twice, but were rotated 180° between tests. Steel wool was used to remove burrs and to polish the rails after the first use.) To minimize contact resistances, the rails were cool-amped (silver plated) at the breech end. The accelerator was assembled, and the clamping bolts were tightened with a torquing wrench to 33.9 N m (25 ft lb). The rail accelerator then underwent a high-voltage stress test (high-potting) to 5 to 10 kV. After the projectile was positioned and all instrumentation installed, the assembly was rolled into the test chamber. Once instrumentation lines had been connected, the test chamber was evacuated by a roughing pump to the desired tank pressure. Following final checkout of the data recorders (oscilloscopes and cameras), the capacitor banks were charged via the control console. The rail accelerator was fired by a manual trigger on the console.

Test Results and Discussion

This section presents the results of 145 rail accelerator tests. Pertinent information on experimental conditions, projectile characteristics, and overall accelerator performance is summarized in tables. The tables are categorized by rail accelerator design and/or test objective. The test numbers were assigned in chronological order.

Tables I and II give data on the performance of the small- and medium-bore rail accelerators. The results of tests 105, 111 to 112, and 126 will be explained in detail. Table III presents the results of the intentional plasma blowby tests in which grooves of various depths were cut in the sides of the projectile. Table IV details test results in which an unconfined plasma armature (no projectile) was accelerated. Some tests are excluded from the tables because of insufficient or highly questionable data. Test numbers highlighted with an asterisk indicate the use of new G-10 structure pieces.

Streak-camera photographs of the intentional blowby series of tests with the medium-bore rail accelerator are presented in appendix B.

Also included in the appendixes are two items of general interest. Appendix C describes a photonic sensor technique for measuring bore pressure. Appendix D describes the use of a high current ignitron (closing switch) in crowbar service in the NASA Lewis pulsed-power system. The resistance characteristics of the ignitron and their impact on pulse shaping will be discussed.

Small-Bore Rail Accelerator Tests

Table I presents the test results of the three small-bore rail accelerator structures. The test objectives were to find a structural configuration that could withstand the loading stresses due to a 200-kA peak current without material failure and give nominal performance, that is, have an effective inductance gradient which approaches the L' for ideal Lorentz force acceleration. For the small-bore rail accelerators, the calculated L'_{av} value of 0.52 μH/m was used as the measure of theoretical expectations.

Both the design C (composite tube) and design D (double-squeeze configuration) rail accelerators survived peak currents to 230 and 192 kA, respectively, without exhibiting structural fatigue and/or material failure. None of the designs achieved nominal performance. Figure 14 plots L'_{eff} as a function of peak current level for the three designs. All L'_{eff} values fall well below the nominal performance value of 0.52 μH/m and, in fact, are typically less than 20 to 40 percent of the theoretical expectations. The effective inductance gradient decreases sharply with increasing peak current level (stress load) and, in general, with the number of successive test firings.

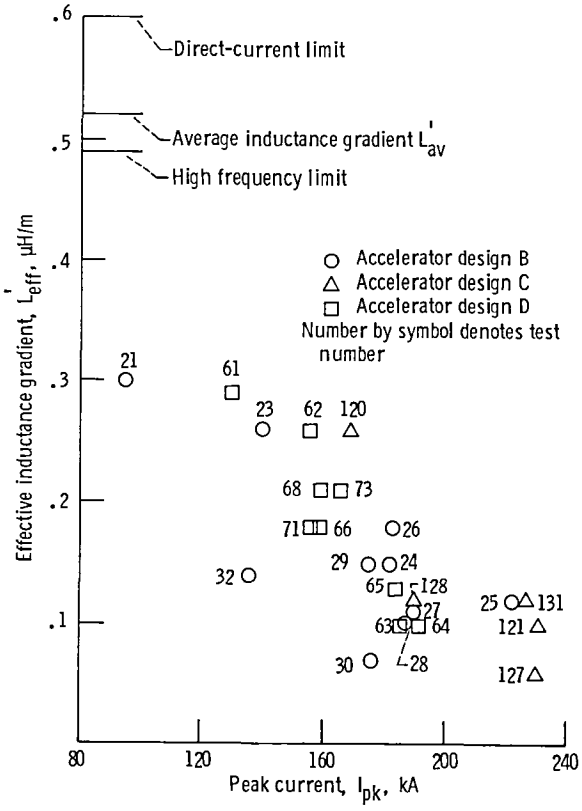

Figure 14.—Effective inductance gradient as function of peak current for 1-m-long, small-bore rail accelerators.

TABLE I.—SMALL-BORE RAIL ACCELERATOR TEST RESULTS

Test (a)	Total capacitance, C, mF (b)	Total inductance, L, μH	Charge voltage, kV	Fire voltage, kV	Crowbar time, μsec	Peak current I_{pk}, kA	Time to peak current, t_{pk}, msec	Projectile design (c)	Projectile mass, g	Start position, cm	Breech plug	Outer structure or backing plate material	Tank pressure, kPa	Tank pressure, Torr	Blowby observation	Blowby velocity, m/sec	Final projectile velocity, v_f, m/sec	Time for projectile to exit muzzle, t_f μsec	Action, A^2 sec	Effective inductance gradient, L_{eff}, μH/m
1-m-long; design B																				
21*	1.265	1.5	4.27	3.82	70	95	63	Standard	0.168	2.54	No	-------	100.5	754	Light	2500	1050	1000	1.2×10^6	0.30
23			6.32	5.85		140	63		.168			-------	99.9	749	None	N/A	1930	530	2.5	.26
24			8.09	7.60		182	63		.173			-------	99.6	747	Very light	3500	2083	483	4.8	.15
[d]25			9.33	8.94		212.5	60		.169			-------	99.1	743	Moderate	3400	2273	440	6.4	.12
26			8.11	8.02		183	60		.183			-------	99.1	743	Light	2780	2170	470	5.5	.18
27			8.15	8.12		190	58	Grooved	.150			-------	98.7	740	Light	3530	2080	500	5.6	.11
28			8.17	8.08		187	58	Undersized	.138			-------	98.5	739	Light	----	1722	450	5.0	.10
29			8.10	8.05		175	60	Standard	.181	50.0		-------	99.1	743	Heavy	2353	1983	412	4.9	.15
30			8.12	8.04		176	60	Standard	.169	50.0		-------	96.9	727	Heavy	3067	1000	470	4.8	.07
32			6.42	6.36		136	62	Standard	.173	2.54		-------	98.8	741	Heavy	3330	1200	600	2.6	.14
3-m-long; design B																				
123	3.80	12.7	10.37	10.26	330	160	330	Standard	.204	10.0	Yes	-------	26.7	200	(e)	2667	3168	1150	18.3×10^6	0.07
124	3.80	12.7	8.39	8.33	330	130	330	Standard	.202	10.0	Yes	-------	26.0	195	(e)	1839	3568	1200	13.0	.11
1-m-long; design C																				
[f]120	1.265	1.6	6.77	6.68	70	169	69	Standard	0.204	10.0	Yes	G-10	25.9	194	None	----	2570	460	4.06×10^6	0.26
121			9.51	9.41		231	70		.205			G-10	26.7	200	Heavy	2941	1800	650	7.27	.10
127			9.50	9.39		230	70		.196			G-10[g]	26.1	196	Heavy	[h]6900/3220	1402	580	8.8	.06
128			7.83	7.75		190	70		.199			G-10[g]	26.7	200	Heavy	4286	1852	544	5.88	.12
131*			9.49	9.37		227	70		.200			Carbon and G-10 composite	26.7	200	Heavy	8000	2400	520	8.32	.12
1-m-long; design D																				
61	1.265	1.6	6.43	6.38	70	130	65	Standard	0.165	10.0	Yes	Phenolic	26.1	196	Very light	2820	2075	540	2.4×10^6	0.29
62	1.265		8.07	7.52		156	65		.171			Phenolic	27.3	205	None	----	2610	440	3.4	.26
63	1.270		9.42	8.88		186	69		.168			MS/SS[i]	28.1	211	Heavy	4348	1485	660	5.2	.10
64	1.265		9.40	8.90		192	65		.168				26.8	201	Moderate	4340	1754	600	6.2	.10
65			9.38	8.90		184	70	Scooped out	.154				28.0	210	Moderate	4880	2130	530	5.1	.13
66			8.15	7.58		159	65		.168				26.9	202	Moderate	3300	1960	510	3.7	.18
68			8.13	7.56		159	68		.162				27.7	208	Heavy	7400	2417	420	3.7	.21
71			8.02	7.54		156	65		.161			Phenolic	26.5	199	Very light	2833	1952	475	3.4	.18
73			8.10	8.01		166	68		1.95			Phenolic	26.5	199	Heavy	4000	2000	470	3.8	.21

[a] Asterisks denote new G-10 structure pieces.
[b] Calculated.
[c] See fig. 8.
[d] Onset of crack formation.
[e] Secondary arc behind projectile.
[f] Second test with this G-10 structure.
[g] Fiberglass faced off further to provide wider clamping surface.
[h] Two blowby arcs.
[i] Mild steel outer and stainless steel inner; torque, 54.2 N M (40 ft lb).

Three primary reasons are believed to be the cause of low performance: (1) ablation of the rail and sidewall materials, leading to plasma deceleration (refs. 21 and 22); (2) compression of the barrel structure (G-10 insulation), leading to plasma blowby and gas-pressure leakage; and (3) progressive crack formation and delamination of the barrel material leading to plasma blowby and gas-pressure leakage (design B only). The ablation phenomenon will be described more fully in the next section. The latter two causes for low performance are directly related to the material strength properties of the accelerator structure and its ability to maintain mechanical integrity (tight bore seal) under impulsive loading.

The large rail forces (10^4 to 10^5 N) at the breech of the rail accelerator cause outward displacements of the structure materials (rails, G–10, and phenolic). The rail displacement has been calculated as high as 0.06 mm (ref. 23). Even though the compressive strength of the G–10 was not exceeded, this rail displacement compressed the G–10 insulation against the backing plates. Additionally, the G–10 was subjected to high shear forces and tension that in some cases (with design B) resulted in material failure. Because of the material compression and/or failure, gaps were created not only between the projectile and the rail or sidewall materials, but also between the mating surfaces of the G–10 structure pieces.

Plasma blowby occurs when gas-pressure forces the plasma through the gaps between the projectile and rail surfaces. If sufficient plasma blows by the projectile, a secondary arc will strike in front of the projectile, reducing the force available for acceleration. Analysis of dB/dt probe data and fiber optic data indicate that a significant portion of the current is diverted through this secondary path. Gaps between the mating surfaces of the G–10 insulation allow gas-pressure leakage during acceleration, further degrading rail accelerator performance. It is not known how this gas-dynamic pressure leakage affects the stability and uniformity of the plasma pressure exerted on the backface of the projectile.

Figure 15 illustrates the effects of the magnetic repulsive forces that must be contained. The small-bore, design B, rail accelerator is shown after successive tests at peak currents from 175 to 212 kA. High shear forces along the inside curved surface near the accelerator breech resulted in progressive crack formation and eventual delamination of the G–10 insulation. The figure also shows the presence of a black sooty deposit between the fiber layers, which indicates gas-pressure leakage during acceleration. Surface analyses have shown this residue to be composed of mostly copper oxides and carbon (refs. 8 and 24).

Because the limitations of the parallel-to-fiber G–10 mechanical strength properties were avoided with designs C and D, the rail accelerator structures did not fracture materially under impulsive loading. However, neither of the designs maintained a tight bore seal under impulsive loading. The in-bore instrumentation indicated severe plasma blowby for most of the test firings. Also, inspection of the accelerator structure after each test revealed excessive black sooty deposits on all mating surfaces of the G–10 for both designs. It appears that even though the clamp design is sufficient to contain the repulsive rail forces, the accelerator insulation pieces compress enough under impulsive loading to permit plasma blowby and gas-pressure leakage. The tests with the design C and D rail accelerators, which exhibited no material failure, indicate that compression of the barrel structure is an ultimate design limitation of rail accelerators.

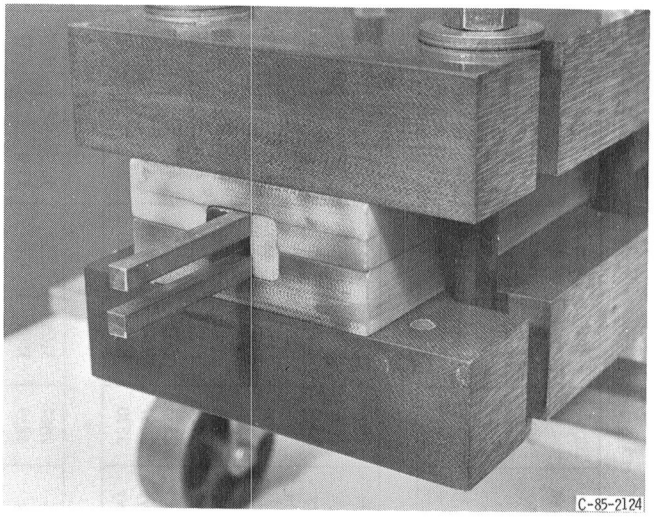

Figure 15.—Breech end of the small-bore rail accelerator—design B.

Medium-Bore Rail Accelerator Tests

The 1-m-long, medium-bore rail accelerator was designed with clear polycarbonate sidewalls so that plasma armature acceleration could be observed. The test objectives were (1) to photograph the plasma armature during acceleration, (2) to measure performance (L'_{eff}) as a function of peak current (stress load), (3) to quantify the effect of plasma blowby on performance, and (4) to study the effect of bore pressure on plasma-driven projectile acceleration and on unconfined plasma acceleration (no projectile). Since high velocity was not an objective with the medium-bore rail accelerator, the current pulse was not matched to the accelerator length; as a result, the current often decayed to zero before the projectile exited the muzzle.

This section presents, first, a representative rail accelerator test to provide a description of arc and projectile acceleration dynamics; next, performance trends for the medium-bore rail accelerator; a test history of one rail accelerator showing lower performance as structure changes occur; and finally, a description of the results of a specific test performed to gain a better understanding of plasma acceleration processes and observed phenomena. These series include intentional plasma blowby, plasma blowby reduction, and unconfined plasma acceleration.

A representative test. – Arc and projectile dynamics and in-bore processes are described for a typical rail accelerator test (test 105) at a 225-kA peak current. Total circuit capacitance and inductance were 2.54 mF and 1.4 μH, respectively. The

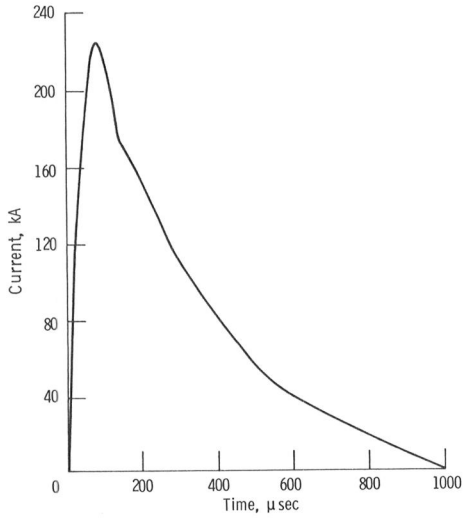

Figure 16.—Representative current versus time profile (test 105).

test chamber was evacuated to 46.4 kPa (348 torr; 0.5 atm) before the firing. The capacitor banks were charged to 5.91 kV and dropped to 5.86 kV at fire. The resulting current waveform is shown in figure 16, with the peak current occurring at 90 μsec. Total action $\int_0^{t_f} I^2\ (t)\ dt$ for this test is 9.65×10^6 A^2 sec.

Figure 17 displays experimental data for the test. The streak photograph of figure 17(a) provides a qualitative description of plasma armature acceleration as well as position-time data. The vertical increments on the photograph indicate distance along the accelerator. A 100-μsec time interval is shown. The streak-camera data, corrected for parallax, along with the other position-time data, are plotted in figure 17(b). The shaded area corresponds to the region of most intense arc luminosity. This region also carries the largest portion of current density as evidenced by corresponding dB/dt probe data points.

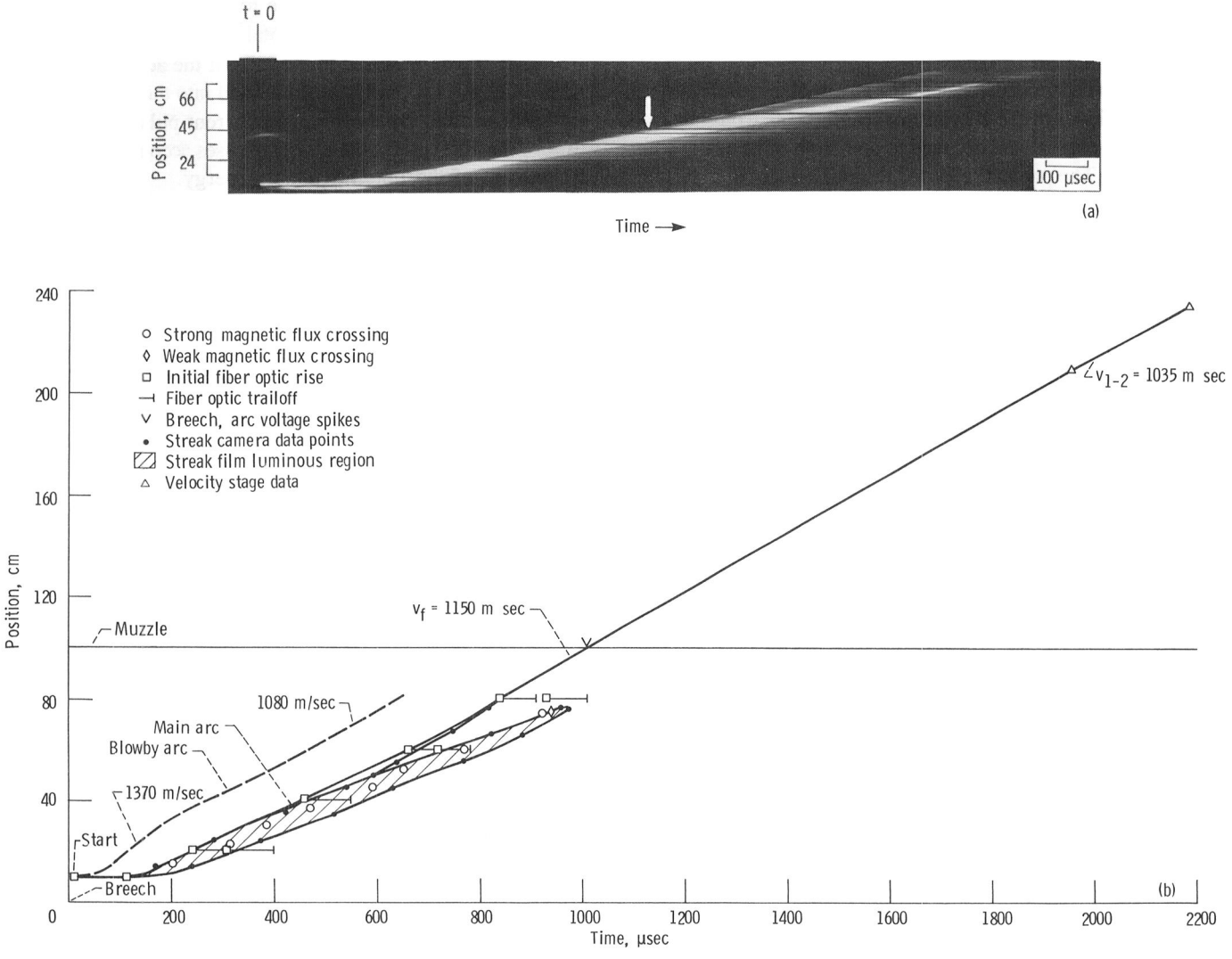

(a) Streak photograph of arc acceleration. Arrow indicates first sign of decoupling of arc from projectile.
(b) Position versus time plot.

Figure 17.—Experimental data for representative test (105).

When the bank was fired, the fully ionized plasma was initiated at the location of the aluminum foil (projectile start). Gas pressure expanded the arc, pushing the projectile forward and the gases rearward. This backward arc motion can be seen more clearly in figure 17(a). Initially (0 to 30 μsec), the gas-pressure forces were greater than the magnetic forces since the current was still low. The current did not reach its peak value until 90 μsec. During this time interval 0 to 90 μsec the arc moved forward less than 1 cm. The plasma arc remained confined initially and then increased in length as its velocity increased. The centroid of the arc was located approximately halfway along the arc length. The *dB/dt* probe data points, which mark the arc centroid location, fall slightly behind the fiber optic data points, which are plotted for the arc wavefront. As arc acceleration progresses the *dB/dt* data fall farther behind the fiber-optic data. The fiber optic data, then, are a better indicator of actual projectile position while in the bore. For this test, the arc half-length increases from 1 cm initially to approximately 8 cm midway. This 8-cm value is in good agreement with theoretical predictions of arc length (authors' calculations and ref. 14).

The projectile stopped accelerating at $x = 60$ cm and coasted for the remainder of the accelerator length. This would be expected as the current had decayed to one-tenth of its peak value at this point. The projectile exited the rail accelerator muzzle at 1010 μsec with a final velocity of 1150 m/sec. The position-time profile of the in-bore data fits in well with the velocity stage timing marks.

The streak photograph of figure 17(a) also shows a faint, luminous wavefront in front of the projectile (precursor). This precursor is caused by the compression of air in front of the projectile. The air was partially warmed by the hot plasma that leaked past the projectile (plasma blowby), as compression alone should not be enough to bring the air to luminous temperatures. Little actual current, though, is associated with this particular wavefront as the *dB/dt* probes did not sense a flux change. This indicates that the amount of plasma blowby in this case was insufficient to strike a secondary arc in front of the projectile.

The streak photograph reveals a second interesting phenomenon. At a position 47 cm downstream of the accelerator breech, there is a distinct split between projectile motion and the arc centroid path. The arc has uncoupled from the backface of the projectile and is decelerating. An arrow indicates the first sign of uncoupling. Arc deceleration may have begun earlier but was too small to resolve optically. One possible explanation for this phenomenon will be presented in a later section.

Rail accelerator efficiency and performance.—From an energy-efficient propulsion standpoint, even though a rail accelerator may perform as expected, overall efficiency is low in that only a small fraction of the initial available energy is converted into the final kinetic energy of the projectile. This low efficiency is mostly due to resistive losses in the arc and rails and partly due to the fact that the current pulse shape may not be tailored to the accelerator length.

Test 105 was chosen as a representative firing because it had good nominal performance; that is, the measured L'_{eff} of 0.43 μH/m matched the theoretical value for the test. In other words the projectile achieved the theoretically estimated velocity predicted by the impulse to the rail accelerator (action).

Figure 18 describes the partitioning of initial energy for test 105. As the capacitor banks discharged, a major portion of the delivered energy was stored temporarily in the total inductance of the circuit, that is, $\frac{1}{2}LI^2$. The stored inductive energy reaches a maximum at the time of peak current and then begins to decrease with time even though the total circuit inductance is increasing due to the accelerator load. Initially, the resistive energy losses, that is, $\int I^2R\,dt$, were low and were due primarily to the resistance of the circuit and of the plasma arc. However, the cumulative resistance losses rapidly increased. For example, by $t=400$ μsec, 37 kJ of the initial 43.5 kJ has been lost due to resistance. At that time 5.4 kJ remained stored in the total inductance of the circuit (less than 0.5 kJ is stored in the rails of the accelerator). Approximately 1.1 kJ had been converted into the kinetic energy of the projectile. By the time the current pulse had decayed to zero ($t=1000$ μsec), the resistive losses accounted for nearly 97 percent of the initial available energy.

It should be noted here that the low, overall efficiency is specific only to this single-stage accelerator configuration and current pulse shape. Significantly higher efficiencies (as high as 40 percent) are possible with the use of optimum pulse shaping and higher projectile velocities.

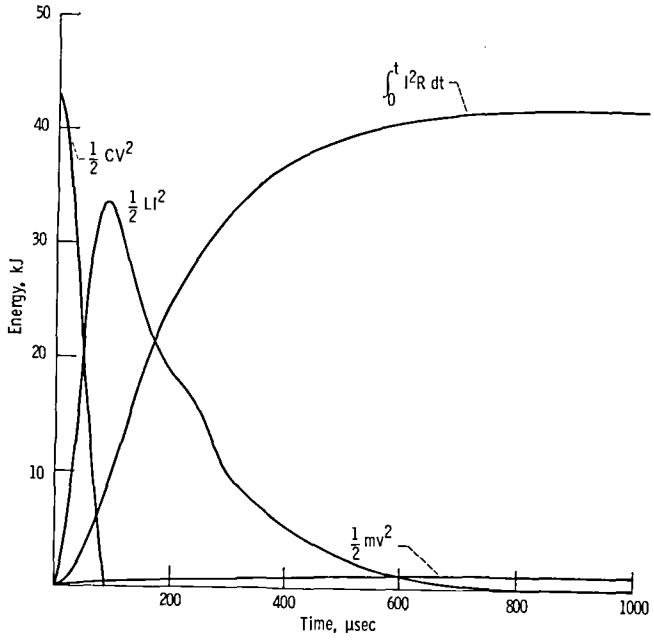

Figure 18.—Energy partitioning for representative test 105.

Arc decoupling and deceleration phenomenon.—Use of streak camera photography (fig. 17(a)) with the medium-bore rail accelerator revealed that the plasma armature uncoupled from the rear of the projectile and decelerated. One possible explanation for this deceleration phenomenon has been proposed by Parker et al. (refs. 21 and 22). Radiation from the high-temperature (10^4 K) plasma arc ablates rail and sidewall material and ionizes it (ref. 21). The mass addition of ionized particles to the arc and projectile system splits the Lorentz force between projectile acceleration and mass addition. Specifically,

$$F = \frac{d}{dt}[(m_p + m_a) \cdot v] = (m_p + m_a)\frac{dv}{dt} + v \cdot \frac{dm_a}{dt} \tag{4}$$

where m_p and m_a denote the projectile and arc masses, respectively. The derivative $dm_p/dt=0$, assuming constant projectile mass.

Ablation of the bore material may not, in itself, be detrimental to plasma armature acceleration. Any addition of ionized, ablated material to the arc, however, affects the current density distribution in the armature and, hence, the Lorentz force. Parker et al. (ref. 22) state that ablation of material from the bore walls may well be the most important limitation to accelerator performance in that it sets a maximum velocity that can be achieved for a given rail geometry and current that is independent of projectile mass.

In addition to the streak-camera photographs, the results of the rail accelerator tests at NASA Lewis provide other evidence which tends to support the above theory. Examination of the copper rails after each test firing revealed arc track marks along the length of the rails, indicating that the arc does remove mass from the rails during acceleration. Significant surface damage to the rails was found at the projectile starting position where the contact time is longest. Figure 19 shows rail damage after a typical firing at a 230-kA peak current. Comparison of signal intensities from two fiber optic probes (with and without copper band pass filters) placed at the rail accelerator muzzle showed strong relative copper line intensity immediately behind the projectile. The intensity from the fiber optic probes, which filtered out the copper lines, decreased rapidly, while the overall, unfiltered intensity decreased slowly. This observation strongly suggests appreciable copper presence in the plasma armature. Further, investigations of rail surface damage have shown that the foil used to initiate the plasma armature plates out on the rail surface soon after arc initiation (ref. 24).

Performance trends for the medium bore rail accelerator.—Data for the 1-m-long, medium-bore rail accelerator tests are given in table II. Figure 20 plots the performance parameter L'_{eff} for each of the tests as a function of peak current level. Each symbol in the figure denotes a separate rail accelerator structure (different G–10 pieces). The number by each symbol denotes the test number. Typical L'_{eff} values range from 0.30 to 0.43 μH/m. Overall, the design gave much better performance than any of the small-bore rail accelerator configurations, not only in terms of percentage of theoretical expectations (70 to 100 percent), but also on an absolute scale.

The large dispersion of data over the range of peak current levels tested delineates no clear pattern for accelerator performance as a function of peak current and/or with the number of tests (structure fatigue). The addition of 4.8-mm-diameter bolts in the outer G–10 structure pieces (tests 49 and later) did help to prevent, or at least postpone, the onset of material failure of the G–10 insulation due to shear stress and tension. Nevertheless, crack formation and delamination of the G–10 structure occurred at peak currents above 200 kA without bolts and above 230 kA with bolts.

The test history of one specific rail accelerator structure sheds more light on the degradation of performance with structural fatigue. Figure 21 details the test history of one medium-bore rail accelerator with the addition of 4.8-mm bolts to reinforce the G–10 insulation pieces. The first three tests (76 to 78) were conducted at a 244-kA peak current. Little plasma blowby was observed, and the rail accelerator gave nominal performance (L'_{eff} = 0.36 to 0.41 μH/m). The rail accelerator was then used for a series of tests from a 100- to 200-kA peak current with a solid copper armature instead of a plasma. (This test series is not discussed in this report; however, the usage data of the accelerator structure are included for completeness.) On the seventh test (solid armature test 82) at 104 kA peak

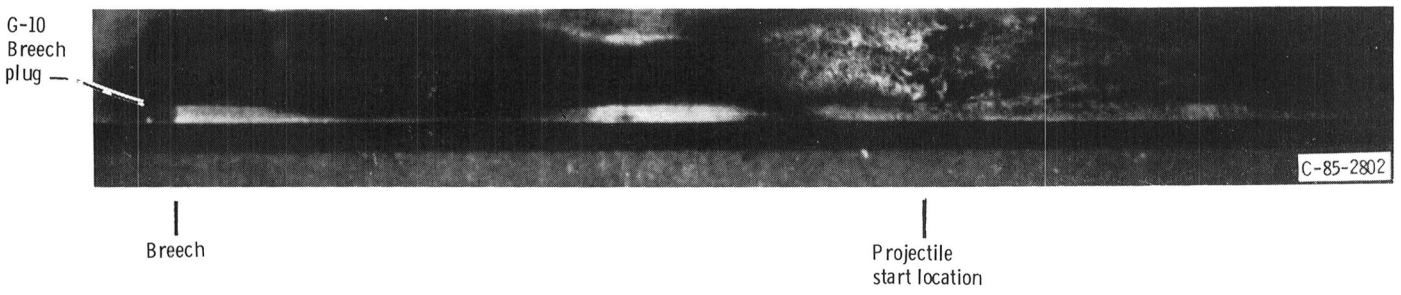

Figure 19.—Rail damage after typical test firing at 230-kA peak current.

TABLE II.—MEDIUM-BORE RAIL-ACCELERATOR TEST RESULTS

Test (a)	Total capacitance, C, mF,	Total inductance, L, μH	Charge voltage, kV	Fire voltage, kV	Crowbar time, μsec	Peak current I_{pk}, kA	Time to peak current, t_{pk}, msec	Projectile design (b)	Projectile mass, g	Start position, cm	Breech plug	Tank pressure, kPa	Tank pressure, Torr	Blowby observation	Blowby velocity, m/sec	Final projectile velocity v_f, m/sec	Time for projectile to exit muzzle μsec	Action, A^2 sec	Effective inductance gradient, L_{eff}, μH/m
[c,d]48	1.265	1.8	10.03	9.62	70	208	75	[e]Double length	2.89	10.0	Yes	26.7	200	Very light	1820	735	1620	8.7×10^6	0.49
[d,f]49	1.265	1.8	10.00	9.61	70	208	75	↓	2.97	↓	↓	26.7	200	Very light	1960	610	1280	8.7	.42
[d]50	2.535	1.2	8.26	7.75	80	242	80	↓	3.02	↓	↓	24.5	184	Heavy	2440	909	1200	14.8	.37
[d]51	↓	↓	7.04	7.00	↓	231	70	↓	1.50	↓	↓	30.3	227	Moderate	3125	1136	950	11.4	.30
[d]53	↓	↓	6.96	6.44	↓	222	80	Standard	1.73	↓	↓	19.9	149	Very light	3290	1192	960	9.8	.42
54	↓	↓	6.90	6.40	↓	219	80	↓	1.70	↓	↓	29.0	218	Light	2222	952	1170	9.4	.33
55	↓	↓	7.03	6.98	↓	232	80	↓	1.65	↓	↓	26.7	200	Very light	2666	1492	800	11.1	.44
56	↓	↓	6.94	6.41	↓	214	75	↓	1.77	↓	↓	[*]27.7	208	Moderate	2440	952	1040	10.3	.33
57	↓	↓	6.92	6.43	↓	210	75	↓	1.75	↓	↓	97.7	733	Light	1667	990	1300	8.4	.41
59	↓	↓	6.87	6.40	↓	210	80	↓	1.61	↓	No	26.4	198	Heavy	3650	877	1200	8.9	.31
[e,g]77	↓	1.4	6.95	6.45	↓	244	85	↓	1.84	↓	Yes	25.6	192	Light	7500	1333	850	12.0	.41
78	↓	↓	6.93	6.43	↓	244	85	↓	1.84	↓	↓	27.5	206	Light	2400	1190	975	12.0	.36
89	↓	↓	7.06	7.01	↓	259	85	↓	1.88	↓	↓	27.3	205	Very light	3570	1538	840	13.2	.44
[h]90	↓	↓	6.90	6.45	↓	244	85	↓	1.97	↓	↓	26.7	200	Light	1430	956	1070	15.6	.38
91	↓	↓	7.06	7.02	↓	264	85	↓	1.75	↓	↓	27.6	207	None	N/A	1715	745	12.6	.36
92	↓	↓	6.95	6.47	↓	243	90	[e]Standard	1.67	↓	↓	27.2	204	Light	4000	1350	950	15.6	.26
[h]93	↓	↓	7.07	7.01	↓	265	85	[e]Standard	3.04	↓	↓	27.3	205	Moderate	2714	667	1540	12.7	.26
[h]94	↓	↓	6.97	6.43	↓	241	85	Standard	3.18	↓	↓	27.7	208	Heavy	3333	526	1870	14.8	.21
[h]95	↓	↓	7.04	6.99	↓	263	90	[e]Standard	1.63	↓	↓	26.8	201	Moderate	3000	935	1090	16.1	.19
[h]96	↓	↓	7.06	7.00	↓	262	87	Standard	1.84	↓	↓	100.3	752	Heavy	2625	778	1250	12.0	.31
98	↓	1.5	6.76	6.45	↓	229	90	↓	1.68	[i]30.0	↓	7.1	53	None	N/A	1308	720	12.2	.36
100	↓	↓	6.93	6.42	↓	240	90	↓	1.76	↓	↓	13.3	100	Moderate	3200	1090	800	12.4	.29
97	↓	↓	6.97	6.44	↓	235	92	↓	1.87	↓	↓	13.6	102	None	N/A	1333	800	12.0	.42
[j]101	↓	↓	7.06	7.00	↓	257	90	↓	1.69	↓	↓	26.5	199	N/A	N/A	1103	840	12.0	.31
99	↓	↓	6.99	6.47	↓	242	92	↓	1.74	↓	↓	100.5	754	Very light	1230	1282	745	12.5	.36
125	1.265	13.5	7.80	7.88	70	71	200	↓	1.65	10.0	↓	46.5	349	None	N/A	628	2130	3.7	.56
126	1.265	1.4	7.85	7.77	70	195	62	↓	1.67	↓	↓	46.5	349	Very light	4400	850	1290	7.1	.40
129	2.535	1.4	5.95	5.88	80	220	90	↓	1.62	↓	↓	46.4	348	Heavy	[k]1944/ 1889	963	1070	10.2	.31
107	↓	↓	5.91	5.87	↓	223	85	↓	1.81	↓	↓	3.6	27	Very light	[k]3338/ 3478	1058	1055	9.72	.40
102*	↓	↓	5.92	5.88	↓	225	90	↓	1.68	↓	↓	6.9	52	Heavy	4421	976	1070	10.8	.30
103	↓	↓	5.93	5.89	↓	226	90	↓	1.80	↓	↓	13.3	100	Very light	2990	1000	1070	10.6	.34
104	↓	↓	5.91	5.88	↓	227	95	↓	1.65	↓	↓	26.1	196	Very light	1530	1273	920	9.9	.42
105	↓	↓	5.91	5.86	↓	225	90	↓	1.82	↓	↓	46.4	348	Very light	1081	1150	1010	9.65	.43
106	↓	↓	5.91	5.87	↓	223	90	↓	1.76	↓	↓	100.0	750	Moderate	1370	996	1080	9.56	.36
108	5.06	13.5	10.43	10.36	380	188	400	↓	1.73	↓	↓	46.3	347	Very light	2000	2028	873	21.8	.33
110	5.06	13.5	10.44	10.39	380	190	400	↓	1.70	↓	↓	46.8	351	Light	1693	1667	920	24.5	.23
109	3.80	1.4	8.47	8.43	120	445	120	↓	1.81	↓	↓	45.9	344	Moderate	6400	2110	575	29.5	.15

[a]Asterisks denote new G-10 structure pieces.
[b]See fig. 10.
[c]Sixth projectile test with these G-10 pieces.
[d]G-10 inner structure pieces. All other tests use Lexguard.
[e]No obturator.
[f]G-10 outer structure pieces strengthened with 4.8-mm bolts.
[g]Second shot with this accelerator.
[h]Severe G-10 cracking.
[i]G-10 cracked at breech; start position moved.
[j]Special test: aluminum foil placed in front and rear of projectile.
[k]Two distinct blowby arcs observed.

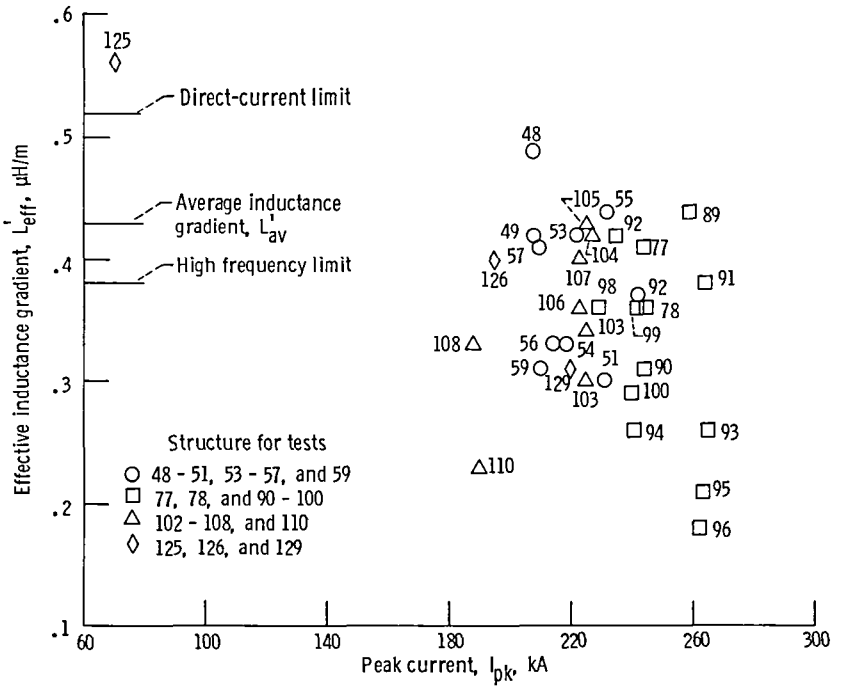

Figure 20.—Effective inductance gradient as function of peak current for 1-m-long, medium-bore rail accelerator.

current, a small crack (a few centimeters long) developed in the bottom, outer G–10 structure piece along a single fiber lamination at the projectile start location. The G–10 structure pieces were then switched end-for-end for the eighth firing so that undamaged G–10 material would be at the breech where the magnetic repulsive forces are greatest. No further crack formation was observed for the remainder of the solid armature test series.

Plasma armature tests with the same rail accelerator structure were resumed with test 89 at 259 kA. The L'_{eff} was nominal (0.44 μH/m). The next test (90) was conducted at a 244-kA peak current. After the firing, 12-cm-long cracks were found on both the top and bottom outer G–10 structure pieces. The cracks were located near the projectile's start position, extending from $x = 11$ to 23 cm from the breech. The G–10 structure pieces were again switched end-for-end (original placement).

Subsequent test firings at 240- to 265-kA peak current brought further crack formation and shifting of the G–10 laminations at both the breech and muzzle ends of the accelerator. Increased plasma blowby and lower L'_{eff} values resulted with each successive test as seen in tests 92 to 96 in

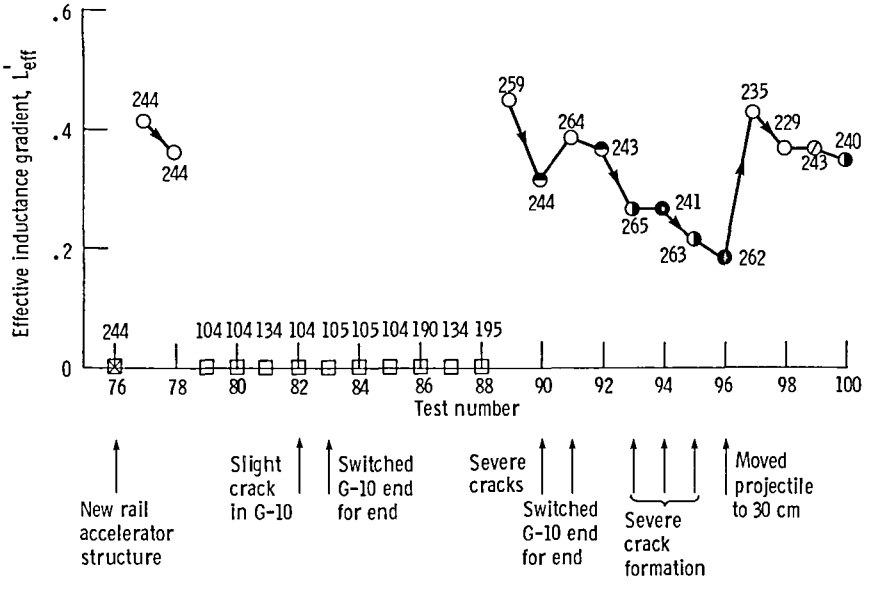

Figure 21.—Test history of 1-m-long, medium-bore rail accelerator with 4.8-mm-diameter bolts.

figure 21. As the G–10 structure fatigued, the outward repulsive forces could not be restrained; gaps created between the rail surface and projectile increased, allowing more plasma to blow by. Tests with moderate to heavy blowby had a significant portion of the rail current flowing through the plasma in front of the projectile. Also, the presence of carbon deposits between the fiberglass laminations indicated that gas-pressure leakage occurred during the test series. For test 97 (the 22nd test firing), the projectile's starting location was moved to a position 30 cm from the breech where the G–10 was still undamaged. At a 235-kA peak current, no plasma blowby was observed, and the resulting L'_{eff} was 0.42 μH/m. The last three tests with this rail accelerator brought slight increases in the amount of plasma blowby observed and corresponding decreases in the performance values.

This particular rail accelerator was used for 25 tests. Test histories with other medium-bore rail accelerators show the same general trends; namely, that low L'_{eff} values are usually accompanied by plasma blowby and, in cases where the G–10 structure has fatigued, evidence of gas-pressure leakage. The detrimental effect of plasma blowby has been observed in similar investigations (ref. 25).

Intentional blowby tests.—Table III summarizes the results of the intentional blowby tests with the medium-bore rail accelerator. The objective of the tests was to examine the effects of intentionally promoting plasma blowby by cutting channels of increasing depths up to 1.42 mm into opposite sides of the projectile (fig. 10 (c)). The test results in table III are listed in order of increasing channel depth and grouped by energy level. Appendix B presents the corresponding streak photographs for the tests.

The first group of intentional blowby tests began with a new rail accelerator structure (tests 111 to 119 and 134). The tests were conducted at an approximately 220-kA peak current and at a 46.7 kPa (350-torr) tank pressure. Test 111 exhibited very little plasma blowby. It has a lower peak current than the other tests in this first set due to a 500-V lower bank voltage at fire. Based on the energy put into the accelerator, though, performance was nominal ($L'_{eff} = 0.37$ μH/m).

The second test (112) had a 0.18-mm-deep channel cut into two side faces of the projectile. This corresponds to an open area of 3.9 mm^2, or about 2.5 percent of the total bore area. As seen in the position versus time plot of figure 22, the test was marked with intense plasma blowby. In fact, the *dB/dt* signals for the blowby arc were stronger than those of the driving armature. Streak camera data are not plotted in the figure but may be found in appendix B. Framing camera photographs of the test, taken every 55 μsec, are shown in figure 23. The projectile is barely distinguishable in frame 6A.

All subsequent tests at this current level (approximately 220 kA) exhibited heavy plasma blowby and produced L'_{eff} values of 0.31 μH/m or less. Tests 113 and 134 had two

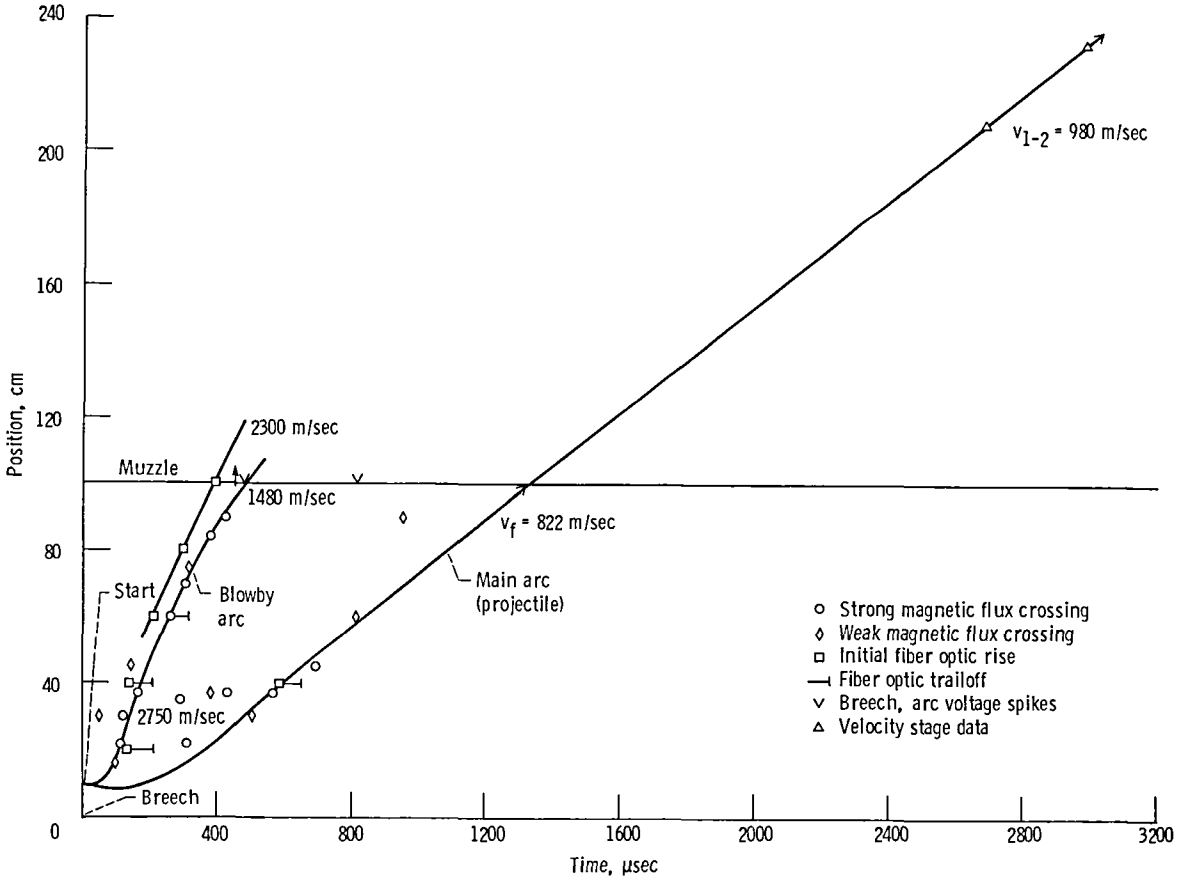

Figure 22.—Position versus time plot for test 112; intentional blowby series. Channel depth, 0.16 mm.

TABLE III—INTENTIONAL BLOWBY RAIL ACCELERATOR TEST RESULTS

[1-meter long, medium-bore; Lexguard sidewalls.]

Test (a)	Total capacitance, C, mF,	Total inductance, L, μH	Charge voltage, kV	Fire voltage, kV	Crowbar time, μsec	Peak current I_{pk}, kA	Time to peak current, t_{pk}, μsec	Channel depth mm	Projectile mass, g	Start position, cm	Breech plug	Tank pressure, kPa	Tank pressure, Torr	Blowby observation	Blowby velocity, m/sec	Final projectile velocity v_f, m/sec	Time for projectile to exit muzzle t_f μsec	Action, A^2 sec	Effective inductance gradient, L'_{eff}, μH/m
111*	2.535	1.4	5.82	5.26	80	[b]198	90	0	1.73	10.0	Yes	46.3	347	Very light	1650	833	1330	7.82×10^6	0.37
119	↓	↓	5.91	5.87	↓	220	90	0.05	1.70	↓	↓	44.5	334	Heavy	2848	895	1420	10.2	.30
112			5.94	5.88		222	88	.18	1.69			46.3	347	Heavy	2077	822	1340	9.3	.30
113			5.94	5.88		221	90	.25	1.57			46.3	347	Heavy	[c]2345/3360	885	1200	9.2	.25
114			5.91	5.86		222	88	.38	1.53			46.9	352	Heavy	5880/1409	855	940	9.3	.31
117			5.93	5.88		220	90	[d].38	1.61			46.5	349	Heavy	2530	882	1190	10.3	.28
115			5.94	5.89		219	↓	.53	1.62			46.5	349	Heavy	3050	837	1310	9.1	.30
116			5.90	5.85		220		.81	1.62			46.4	348	Heavy	4830/2000	840	1330	10.5	.26
134			5.87	5.84		218		[e]1.42	1.96			46.1	346	Heavy	[c]3086/1890	628	1757	10.7	.23
137			5.23	5.19		196		0	[f]1.84			45.1	343	Heavy	2182/1238	667	1500	7.23	.34
136			5.21	5.16		194		0.38	1.58			46.1	346	Heavy	2270	729	1520	7.07	.32
[g]138			5.02	4.98		182		0	1.62			45.9	344	Light	1947	1079	1060	7.8	.45
139			5.02	4.98		186		.18	1.85			46.8	351	Light	2273	856	1310	7.1	.44
140			5.01	4.97		181		.38	1.79			46.0	345	Moderate	1500	714	1400	6.35	.40
141	↓	↓	5.00	4.97	↓	182	↓	.76	1.70	↓	↓	46.1	346	Heavy	[a]3330/1887	680	1460	6.4	.36

[a] Asterisks denote new G-10 structure pieces.
[b] Same initial charge voltage as the other tests in this group.
[c] Two distinct blowby arcs observed.
[d] Channel depth oriented 90° from usual.
[e] No hole drilled into projectile.
[f] Projectile made of black Lexan.
[g] G-10 switched end for end.

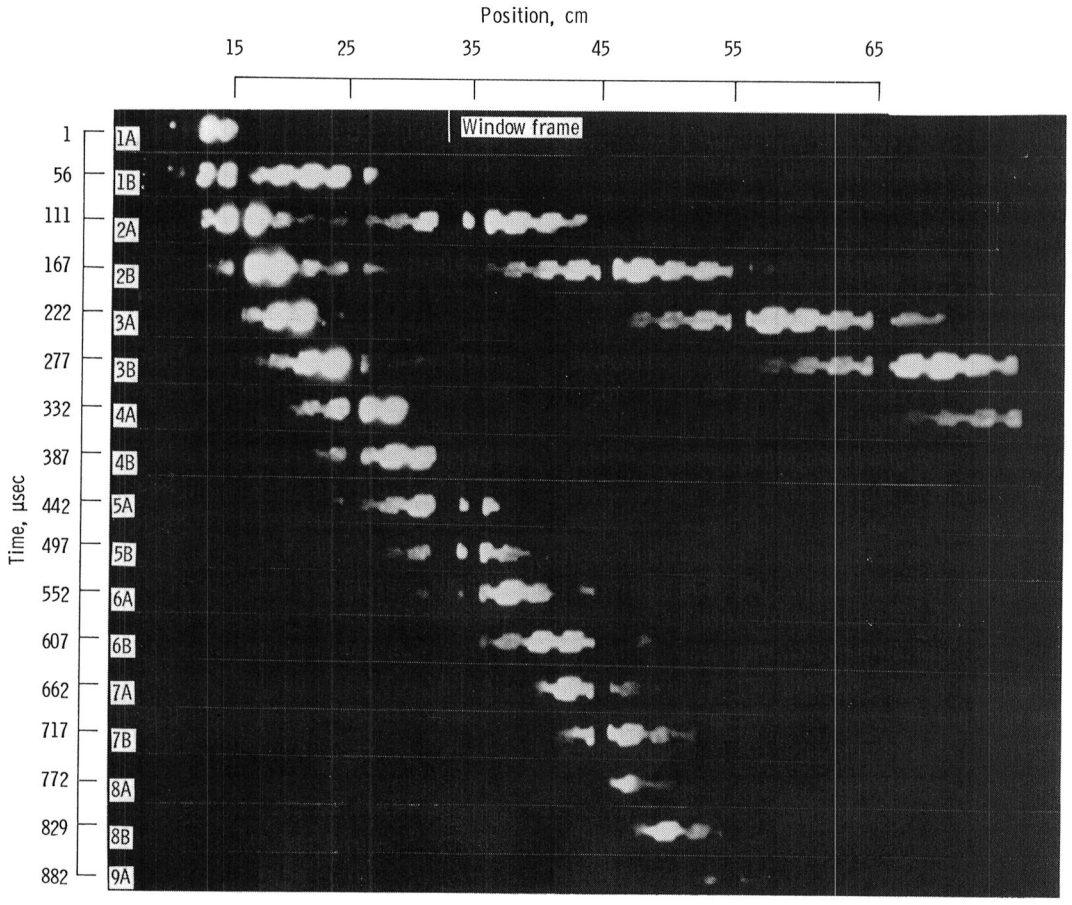

Figure 23.—Framing camera photographs of test 112. Film speed, 18 000 pps; exposure time, 1.1 μsec; no parallax corrections were made on position marks.

distinct plasma blowby wavefronts. These tests gave the worst overall performance with L'_{eff} values of 0.25 and 0.23 μH/m, respectively.

The intentional plasma blowby tests were resumed with the same rail accelerator structure at a lower peak current (approximately 195 kA). By this time, the rail accelerator had been used for 12 tests, and cracks had developed at the breech end of the G–10. Heavy plasma blowby was evident for both tests 136 and 137 but, at the lower peak current level, overall performance values were slightly higher. Test 136 had more arc damage than usual to the rails at the projectile's starting position, suggesting a longer projectile startup time. The streak camera photographs indicate that the plasma armature remained stationary for the first 75 μsec of this test (appendix B).

The G–10 outer structure pieces were switched end-for-end for test 138. With undamaged G–10 at the accelerator breech and a lower peak current (approximately 185 kA), L'_{eff} was 0.45 μH/m. For the next three tests (139 to 141), the amount of plasma blowby observed increased with channel depth. Also, the performance values decreased in direct proportion to the square of the ratio of the unsealed bore area to the bore area. The decrease is proportional to the square of the area ratio because (1) the base area on which the plasma pressure acts is reduced and (2) the plasma pressure is reduced by the unsealed bore area, possibly in direct ratio of base area to bore area. Specifically,

$$L'_{\text{eff}} = L'_0 \left(\frac{A_u}{A_0}\right)^2 \tag{5}$$

where A_0 is the bore area (156 mm^2), A_u is the unsealed bore area (A_0 minus gap clearance area), and L'_0 is L'_{eff} with no clearance.

Figure 24 plots L'_{eff} as a function of increasing clearance depth for the intentional blowby test series. Each symbol denotes a different peak current level, while the shading indicates to the qualitative amount of plasma blowby observed. The solid curves in the figure are given by equation (5), using L'_0 values of 0.45 μH/m for the tests at a 185 kA peak current and 0.37 μH/m for the tests above 195 kA. As seen in the figure, the data are in good agreement with the emperical fit of equation (5) for the tests at 185 kA. For the tests at 195 kA and above, the significantly lower overall L'_{eff} values indicate that some loss mechanism other than the intentional channel depths is contributing to the large amount of plasma blowby observed and the corresponding degradation in per-

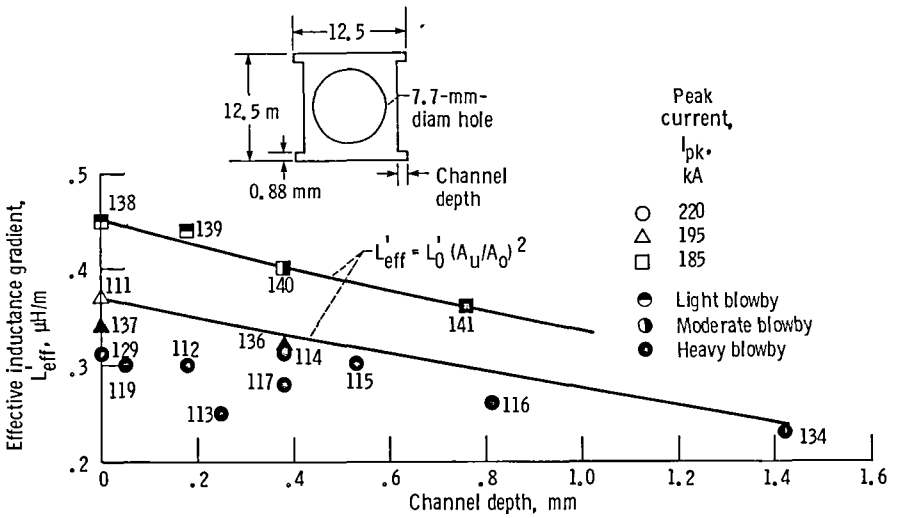

Figure 24.—Effective inductance gradient versus channel depth for the intentional blowby test series.

formance. The fact that G-10 cracks were found during the initial blowby test series (tests 111 to 119) suggests structural fatigue as a possible cause, but it is difficult to draw a definitive conclusion.

Plasma blowby reduction.—At the lower current levels, it was thought that the amount of plasma blowby could be minimized by sealing the bore area between the plasma armature and the backface of the projectile with a black rubber obturator (1.6 mm thick). Comparison of test 126 using an obturator (table II) with test 111 without an obturator (table II) shows only a modest benefit from using this type of obturator. The two tests were conducted at the same peak current level; the impulse to the accelerator (action integral) was comparable. The resulting position versus time plots, along with current and voltage waveforms for the two tests, are presented in figures 25 and 26.

In test 126 with an obturator (fig. 25), the *dB/dt* probes detected no current-carrying plasma blowby. The *dB/dt* probes picked up weak flux changes in test 111 (no obturator) as seen in its position versus time plot (fig. 26). The difference in overall performance for the two cases is slight. The L'_{eff} is 0.40 μH/m for the test with an obturator and 0.37 μH/m for the test without one.

At higher current levels the use of the rubber obturator showed no appreciable difference in the amount of blowby observed and in overall rail accelerator performance. Test pairs 95 and 96, 92 and 78, and 94 and 50 illustrate the minimal benefits of the use of this type of obturator.

Unconfined plasma test series.—Table IV presents tests in which only a foil-initiated plasma armature was accelerated (e.g., no projectile). The purpose of the tests was to examine the acceleration of an arc not constrained by a projectile, such as in the case of an arc created by plasma blowby, and to determine the effects of bore air pressure on the arc acceleration. Further, unconfined plasma velocity represents, in a sense, the maximum velocity that can be obtained for a given impulse input to the accelerator in that the available energy is used only to accelerate the low mass plasma. All of the tests listed in table IV were conducted in the medium-bore rail accelerator except test 34 (small bore, design B). The tests covered a peak current range of 90 to 180 kA and a bore pressure range of 0.53 to 99.0 kPa (4 to 743 torr).

The armature for tests 39, 40, and 42 was initiated with a piece of aluminum foil of dimensions 12.5 by 25.4 by 0.11 mm and weighing 0.096 g. For test 142 to 145, the aluminum foil was approximately half as wide (6.2 by 25.4 by 0.11 mm) and weighed 0.058 g. Test 34 used a foil mass of 0.005 g.

Powell (ref. 26) showed that the effects of bore air pressure are very significant on maximum velocity under conditions corresponding to low masses, high currents, and long time constants. In the case of a nearly constant current, this maximum achievable velocity is proportional to the peak current divided by the square root of the bore pressure. Figure 27 plots the maximum arc velocity of the unconfined arc as a function of $I_{pk}/\sqrt{P_T}$. The maximum arc velocity typically occurred at time $t=100$ to 150 μsec. The arc velocity then decreased (not shown in the figure), presumably because of the presence of air in the bore. It does not seem likely that the arc-ablation phenomenon mentioned earlier could be the cause of the velocity decrease, as the contact time for mass addition to occur is too short (higher velocity). Further, in the case of an unconfined plasma, the maximum arc velocity appears to be relatively mass independent.

The effects of bore air pressure, however, do become insignificant in the acceleration of larger masses, that is, in the case of projectile acceleration. Tests 102 to 107, conducted over a wide range of bore air pressure from 3.6 to 99.8 kPa (27 to 750 torr), support this statement. Data for these tests may be found in table II.

The effects of a transient L'.—It typically takes 920 μsec for the current to diffuse toward the center of the rails of the medium-bore rail accelerator (authors' calculations). It might

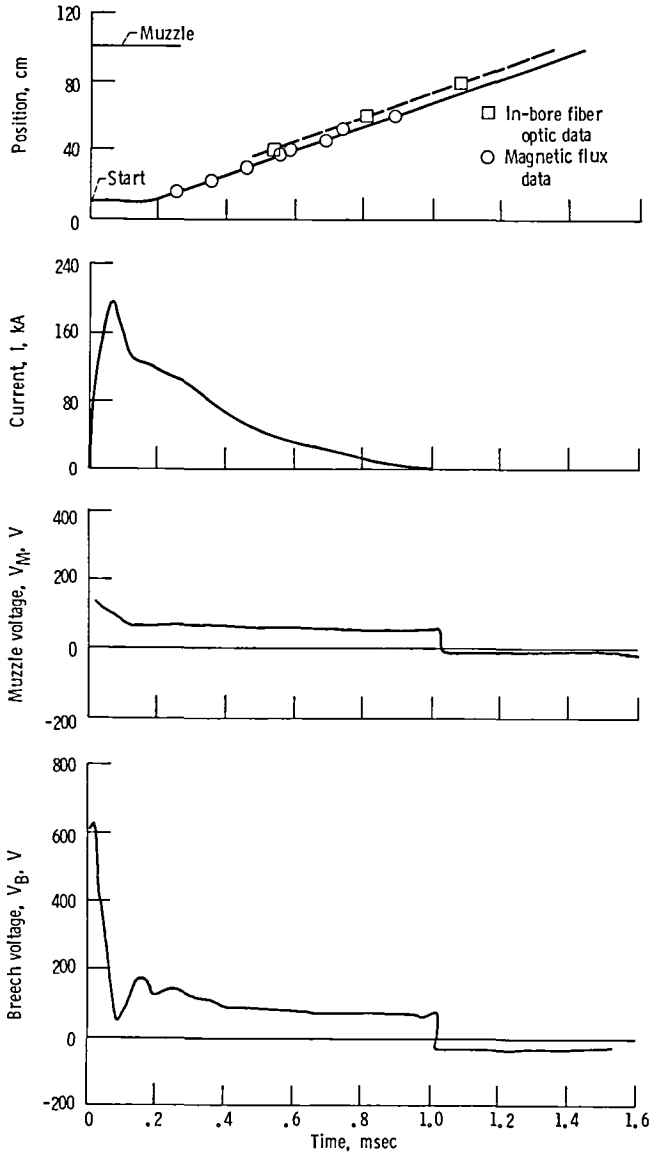

Figure 25.—Waveforms of test firing at 280-kA peak current. Obturator used behind projectile. Test 126.

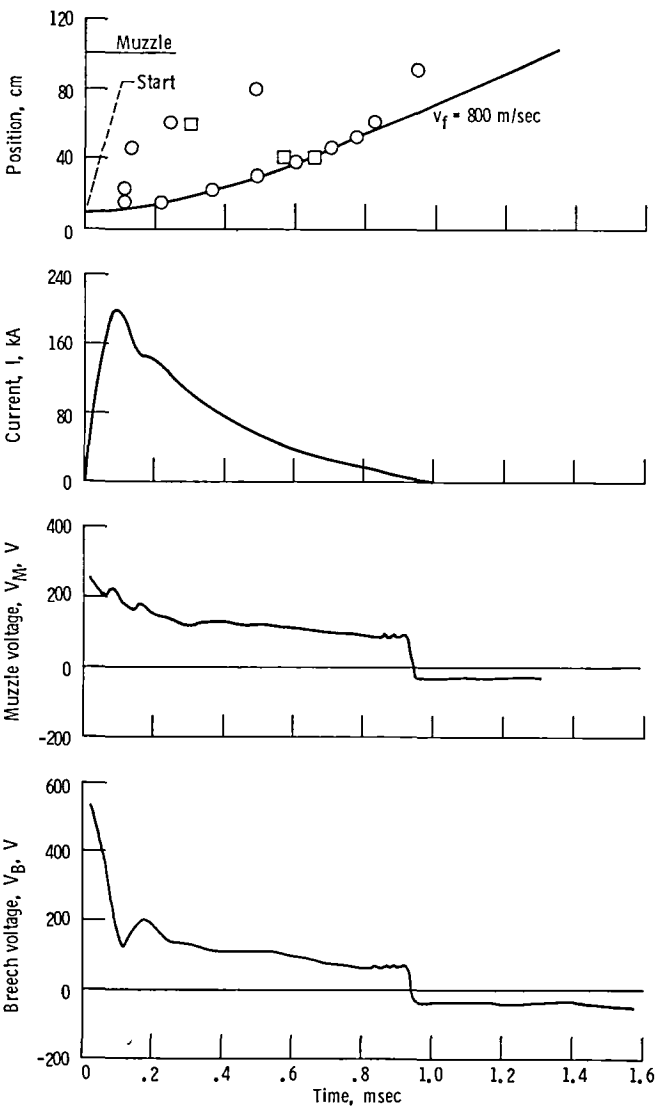

Figure 26.—Waveforms of test firing at 200-kA peak current. No obturator behind projectile used. Test 111.

TABLE IV—UNCONFINED PLASMA

Test	Total capacitance, C, mF	Total inductance, L, μH	Charge voltage, kV	Fire voltage, kV	Crowbar time, μsec	Peak current I_{pk}, kA	Time to peak current, t_{pk}, μsec	Accelerator used	Initial foil mass, g	Start position, cm	Breech plug	Foil mass vaporized (estimated) g	Bore pressure P_T, kPa	Bore pressure P_T, torr	$I_{pk}/\sqrt{P_T}$ kA/(kPa)$^{1/2}$	$I_{pk}/\sqrt{P_T}$ kA/(torr)$^{1/2}$	Arc maximum velocity, m/sec
34	1.265	1.4	6.37	5.88	70	119	65	[a]Small base	[b]0.005	10.0	Yes	0.005	99.1	743	12.0	4.4	3 570
40	↓	↓	4.99	4.49	↓	91	↓	Medium base	[c].096	5.0	↓	[d].016	28.0	210	17.2	6.3	3 704
39	↓	↓	5.05	5.00	↓	102	↓	↓	[c].096	5.0	↓	[e].090	28.3	212	19.2	7.0	4 160
42	↓	↓	7.77	7.73	↓	163	↓	↓	[c].096	5.0	↓	[e].090	28.3	212	30.6	11.2	5 320
145	2.535	↓	5.00	4.96	80	175	90	↓	[f].058	10.0	↓	[f].03	.5	04	240.0	87.5	16 800
144	↓	↓	2.83	2.80	↓	98	↓	↓	[f].058	↓	↓	[f].03	6.1	46	39.7	14.4	5 320
143	↓	↓	5.02	4.98	↓	173	↓	↓	[f].058	↓	↓	[f].03	6.5	49	67.9	24.7	8 930
142	↓	↓	5.00	4.92	↓	179	↓	↓	[f].058	↓	↓	[f].03	25.7	193	35.3	12.9	5 263

[a]Design B.
[b]Aluminum foil (U-shaped).
[c]Aluminum foil (12.5 by 25.4 by 0.11 mm).
[d]Approximately 1/5 of foil mass vaporized.
[e]Al slivers found.
[f]Alumium foil (6.2 by 2.54 by 0.11 mm).

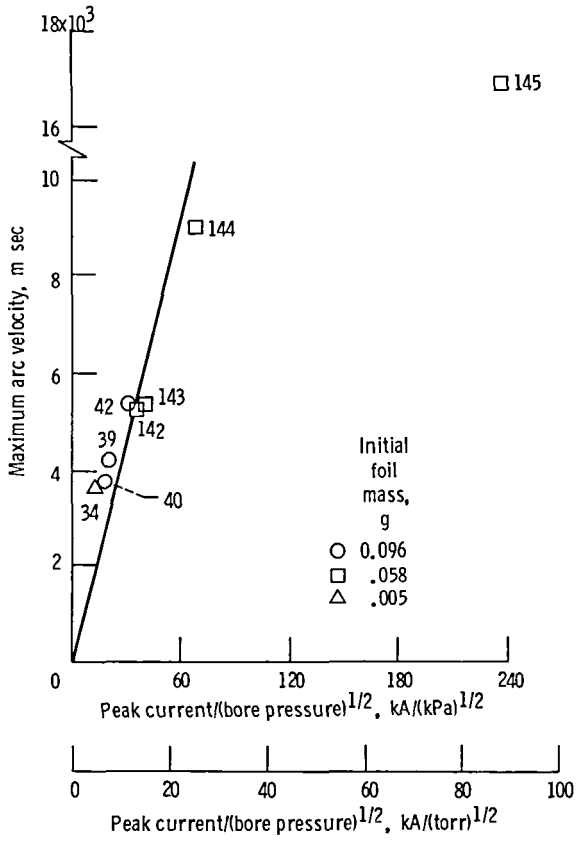

Figure 27.—Velocity of unconfined arc as function of peak current and pressure. The data point for test 145 represents a lower limit to the observed velocity.

be expected, then, that early in the acceleration process the L' available for ideal Lorentz acceleration would be much closer to the high-frequency limit value since electrical skin effects would predominate.

Figure 28 presents an evaluation of the transient performance of five medium-bore rail accelerator tests conducted at different peak current levels. The tests were conducted under similar experimental conditions using a standard-size projectile (fig. 10(a)). All of the tests demonstrated nominal performance, that is, L'_{eff} values greater than 0.40 μH/m and a minimum of plasma blowby. Actual test data may be found in table V (tests 53, 77, 89, 105, and 126).

In figure 28 the performance evaluation is based on projectile velocity at discrete intervals along the accelerator, specifically, at $x = 25$, 40, 60, and 100 cm. Because the impulse input to the rail accelerator also varies, the test data are plotted as a function of action. The ordinant is mass times projectile velocity. The solid line in the figure represents theoretical performance (see eq. (3)) and is given by one-half of the average, instantaneous inductance gradient, $L'_{\text{av}}/2$. The slope of the dashed line is given by one-half of the high frequency limit inductance gradient, $L'_{\text{HFL}}/2$. As seen in the figure, except for a few early data points (at $x = 25$ and 40 cm) that tend toward the high frequency case, nearly all of the data cluster about the line defined by $L'_{\text{av}}/2$.

The average, instantaneous inductance gradient, L'_{av}, has been used as an approximation of anticipated overall rail accelerator performance. Clearly, a more detailed analysis would

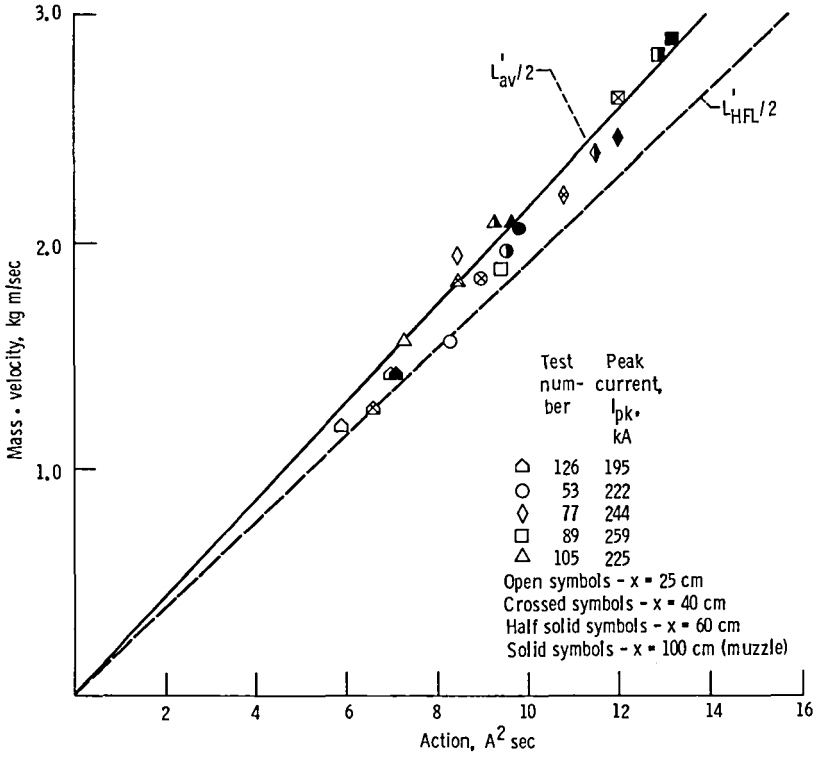

Figure 28.—Time variance of rail accelerator performance. The evaluation is based on data corresponding to discrete intervals along accelerator length.

include the effects of a time-varying L' due to current diffusion into the rails, as has been calculated previously (refs. 11 and 12).

Summary of Results

A rail accelerator research program was conducted at the NASA Lewis with the objective of examining the technical feasibility of using the rail accelerator for large-scale space propulsion applications, including the Earth to orbit delivery of ton-size, nonfragile payloads. Mission studies conducted on contract estimated the cost benefits and evaluated the engineering feasiblity of using the rail accelerator for such applications. A parallel in-house program provided experimental research data with laboratory size rail accelerators of small (4 by 6 mm) and medium (12.5 by 12.5 mm) bores. The in-house program was suspended in October 1984, because the mission studies revealed that the capital expenditure (early investment and construction costs) for an Earth-to-orbit rail launcher cannot be justified unless large amounts of cargo are delivered to space. Such large material delivery requirements were estimated to occur no sooner than 30 years in the future. The results of the in-house experimental program, the subject of this report, delineated new technical problems but did not influence the decision to suspend the program.

The major results and conclusions drawn from the experimental research were

(1) Photographs of the plasma armature acceleration, taken through the clear polycarbonate sidewall of the medium-bore rail accelerator, provided a qualitative description of acceleration as well as information on the length and position of the armature as a function of time.

(2) Overstressing of the bore structure can cause either material failure, and consequently pressure leakage, or sidewall compression, which permits plasma blowby. A significant degradation in overall performance was found as changes in the rail accelerator structure occurred; however, the effects of structural fatigue were not cumulative in a regular and consistent manner. Material compression is one ultimate limit to rail accelerator design.

(3) Ablation and subsequent ionization of the rail and bore sidewall material may cause mass addition to the arc and loss of arc velocity.

(4) The detrimental effects of plasma blowby, pressure leakage, and arc ablation were more prevalent in the small-bore rail accelerators than in the medium-bore configuration.

(5) The medium-bore rail accelerator attained theoretically estimated projectile velocities when operated below critical stress levels.

The authors believe that rail accelerators continue to show promise for future space propulsion mission applications, but continued research is necessary to define and mitigate technical problems. For example, rail accelerator material failures can be avoided by constraining operating stresses within material limits. This defines a maximum operating current level for a specific configuration. Further, because the conversion of energy delivered to a single-stage rail accelerator is low, the above discussion implies that higher projectile velocities will not be attained simply by putting more power into the accelerator. Rail accelerators will have to be made longer and, if necessary, be operated with distributed energy (multistage configurations). Other problems, yet unidentified, may impose operating restrictions sufficiently severe to preclude rail accelerators from certain mission applications. However, there appears to be sufficient promise of large-scale space propulsion applications of the rail accelerator that the concept merits further consideration in the future.

National Aeronautics and Space Administration
Lewis Research Center
Cleveland, Ohio, November 13, 1985

Appendix A
Synopsis of Mission Studies

Three mission studies (refs. 3 to 5) were performed to investigate the technical merit and estimate the cost benefits of using a rail accelerator for a variety of in-space and to-space propulsion applications. The studies contain detailed rail accelerator system designs, mission specifics, and comparisons with alternative propulsion methods. A synopsis of the three studies is included here for background information.

The first study (ref. 3) proposed a continuously firing (5 to 10 Hz) rail accelerator as a means of low-thrust orbit transfer. Gram-sized projectiles, accelerated to velocities of 5 to 20 km/sec, produced reactive thrust for spacecraft propulsion at a power level of 25 to 100 kW_e. Further concept evaluation was discontinued because only a marginal economic advantage existed over ion propulsion systems and because of projectile disposal problems.

The next mission analysis (ref. 4) studied the direct launch of ton-size nonfragile payloads from the Earth's surface to space using a 2-km long, 1 m^2 bore rail accelerator operating in a multistage configuration, that is, with distributed energy totaling 1 TJ (10^{12} J). The study defined and assessed a conceptual Earth-to-space rail launcher (ESRL) system of the 2020 to 2050 time frame capable of fulfilling two candidate missions: (1) deep-space disposal of high level nuclear waste and (2) delivery of bulk cargo to low Earth orbit (LEO). The primary mission required an escape velocity of 20 km/sec at 10 000g's acceleration, while the secondary mission required velocities of 5 to 12 km/sec at 2000g's. With such an ESRL system, as much as (0.5 metric ton) of nuclear waste could be launched into solar system escape at a rate of two launches per day. Approximately 5.2 MT of bulk material could be delivered to earth orbit (eight launches per day).

A follow-on study (ref. 5) emphasized near-term applications, focusing on missions which required the delivery of bulk cargo to space. It considered all types of electromagnetic launcher concepts (EML's), which included, in addition to rail accelerators, the coaxial magnetic accelerator, the electrothermal thruster (ramjet), an electromagnetic rocket gun, and an electromagnetic theta gun. An EML-chemical hybrid was also studied in which the EML served as the first stage (1 to 2 km/sec) and chemical rockets provided the second and third stages. Of all electromagnetic launcher types reviewed by reference 5, only the coaxial magnetic launcher showed promise equal to or superior to that of the rail accelerator.

The mission application chosen for development as a reference concept was the Earth-to-orbit launch of bulk cargo to support an orbiting space station with the delivery of supply items, orbit transfer vehicle (OTV) propellants, and materials for space processing facilities. The mission model assumes a significant manned presence aboard the station by the year 2020.

The Earth-to-orbit rail launcher consists of a multistage, 2-km-long rail accelerator with a 1-m^2 bore. It would launch a 5900-kg projectile (650-kg payload) at 6.9 km/sec at a maximum of 1225g's acceleration. An on-board propulsion system would provide the additional 2 km/sec necessary for orbit insertion at a 500-km altitude.

Both references 4 and 5 concluded that the large-scale mission applications of rail accelerators appear to be not only technically feasible but also economically beneficial. The technology assessments of the two studies found no insurmountable technical barriers to exist and no areas that required a major technological breakthrough; however, substantial extrapolation of the state-of-the-art rail accelerator technology was needed for both the ESRL and the Earth-to-orbit rail launcher concepts. Consequently, the studies identified several critical areas for further research and development. These include (1) the testing of larger rail accelerator systems (to date, rail accelerators that have been tested are typically only a few meters long with centimeter-sized bores.); (2) energy distribution and switching in multistage rail launchers; (3) energy storage; (4) large-scale projectile design; and (5) launcher design.

The economic assessments of the two studies found that the cost benefits of the large scale mission applications are predicated on a large material delivery requirement, that is, high launch rates. This is because of the large capital expenditure (construction costs and early investment). Based on predictions of future space delivery requirements, economic payoff will be post 2020 era.

Appendix B
Photographs of Plasma Acceleration

This section presents streak-camera photographs of the intentional plasma blowby test series (tests 111 to 119, 134, and 136 to 141) with the 1-m-long medium-bore rail accelerator. Plasma blowby was intentionally promoted by cutting channels of increasing depth from 0 to 1.42 mm deep into two sides of the projectile (fig. 10(c)). The streak photographs are listed in order of increasing channel depth and are grouped by peak current level.

The tick marks on the vertical scale of each photograph serve as position indicators. Minor corrections for parallax were made. A 100-μsec time interval is also given for each photograph. Slight variations in the relative length of these intervals is due to differences in the camera film speed during each test. Specific data for each of the intentional blowby tests are given in table III. All tests were conducted at a tank pressure of approximately 50 kPa (350 torr).

For the tests conducted at peak current levels of approximately 200 and 220 kA, no definitive correlation between the amount of plasma blowby observed and the depth of the channel was discerned. All but one of the tests (111) exhibited heavy plasma blowby. This can be seen by comparison of the luminosity of the relatively weak precursor of the streak photograph of test 111 with the other streak photographs in the series. Analysis of the signal strength of the dB/dt probe data indicated that the tests with highly luminous precursors had a significant portion of current flowing through the blowby arcs. For the tests conducted at a 182- to 186-kA peak current, the amount of plasma blowby observed increased with channel depth. However, only the film-strip for test 141 was recovered.

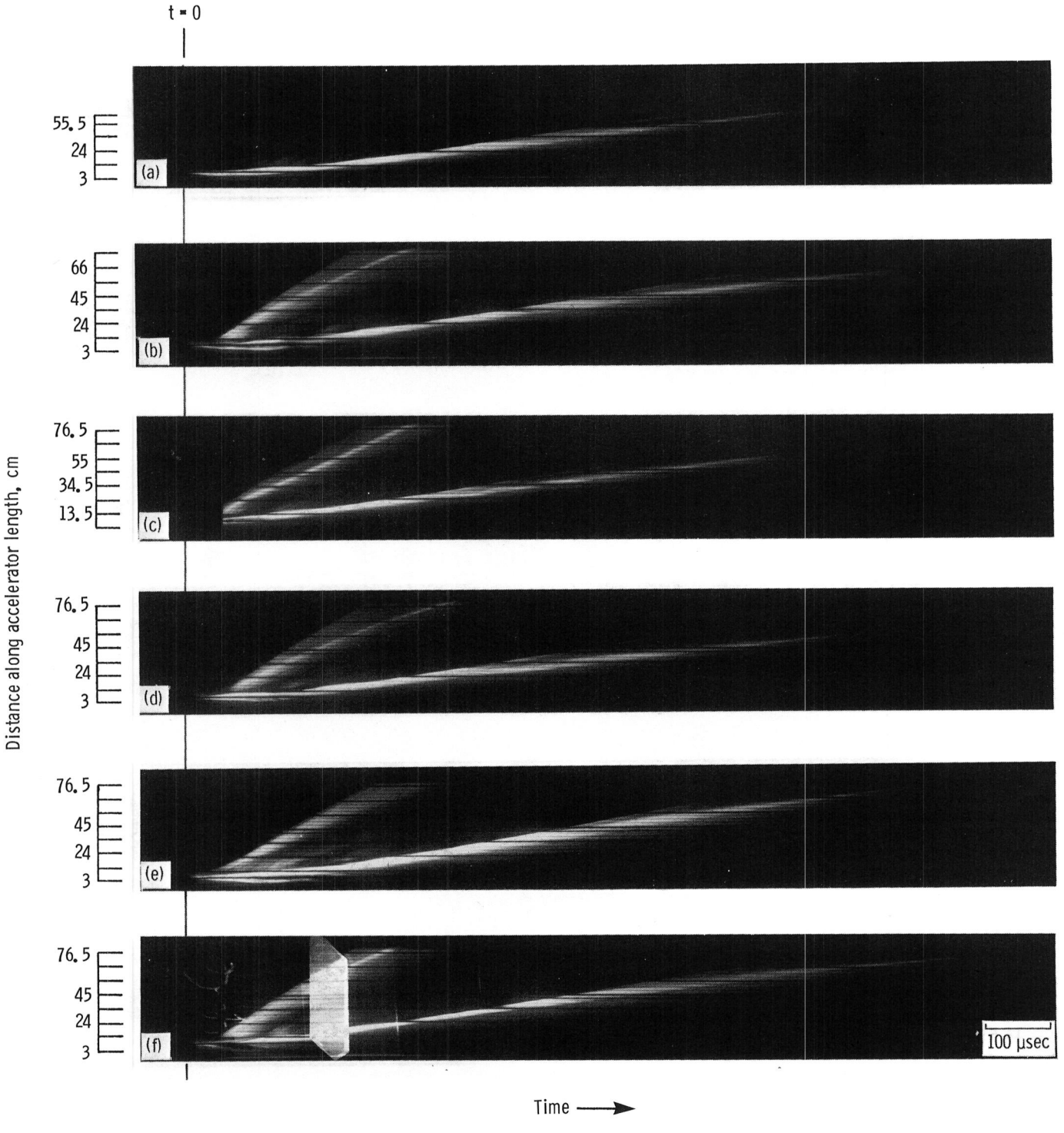

(a) Test 111; channel depth, 0 mm; peak current, 198 kA.
(b) Test 119; channel depth, 0.05 mm; peak current, 220 kA.
(c) Test 112; channel depth, 0.18 mm, peak current, 222 kA. Note: actual starting position not shown.
(d) Test 113; channel depth, 0.25 mm; peak current, 221 kA.
(e) Test 134; channel depth, 1.43 mm; peak current, 218 kA.
(f) Test 136; channel depth, 0 mm; peak current, 194 kA.

Figure 29.—Streak camera photographs.

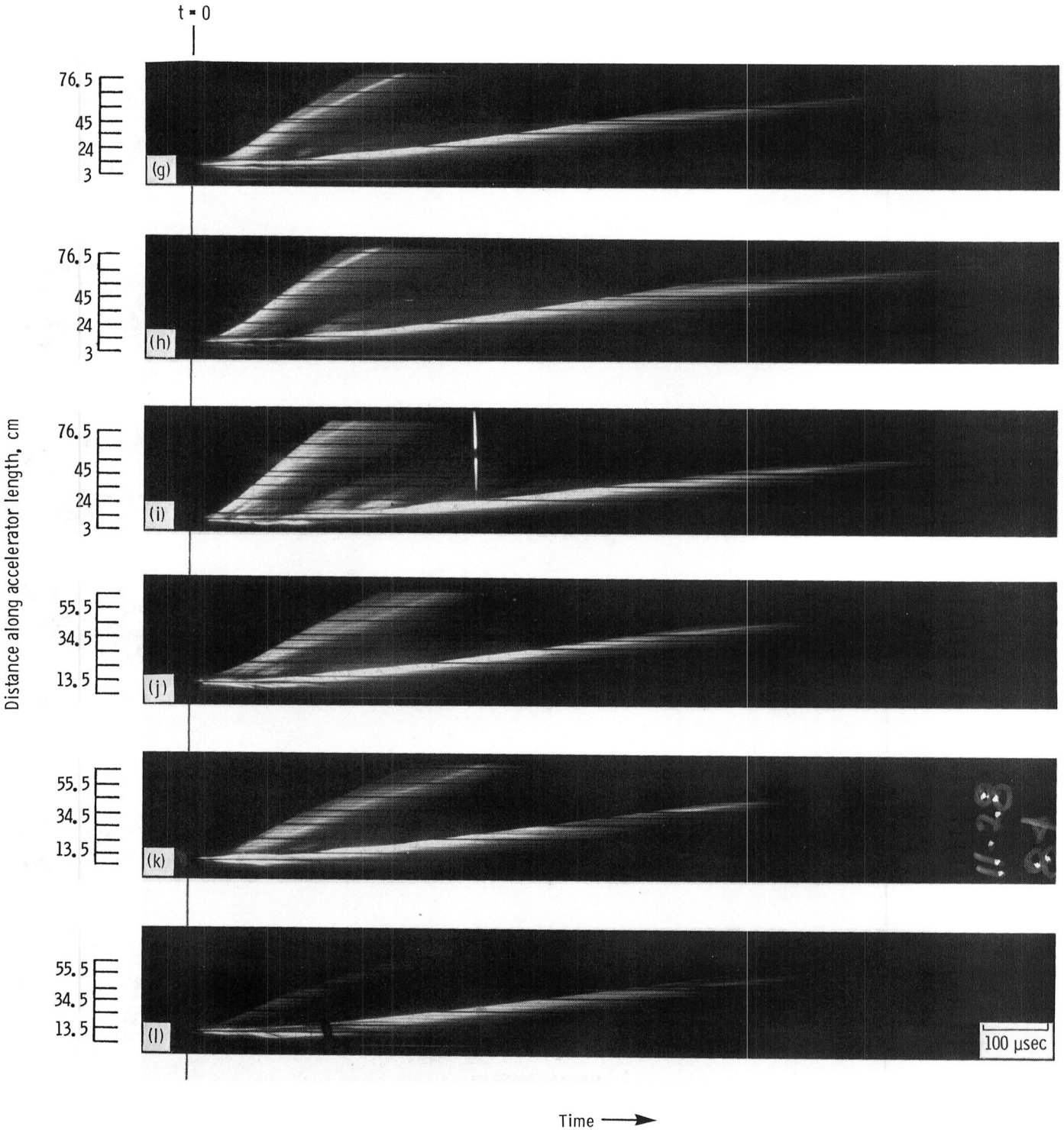

(g) Test 137; channel depth, 0.38 mm; peak current, 196 kA.
(h) Test 141; channel depth, 0.76 mm; peak current, 182 kA.
(i) Test 114; channel depth, 0.38 mm; peak current, 222 kA.
(j) Test 117; channel depth, 0.38 mm; orientation, 90° from usual; peak current, 220 kA.
(k) Test 115; channel depth, 0.54 mm; peak current, 219 kA.
(l) Test 116; channel depth, 0.81 mm; peak current, 220 kA.

Figure 29.—Concluded.

Appendix C
Rail Accelerator Bore Pressure Measurement

One important parameter for both the structural design of the rail accelerator and for analysis of operation is the bore pressure. The measurement of the pressure pulse in the accelerator bore during a test firing is difficult, however, because of the intense electric and magnetic fields produced by the discharge current, which induce spurious signals in any nearby electronic instrumention or wiring. The measurement is further complicated by the initial shock displacement of the entire rail accelerator structure due to the high level energy input. This section describes an optical technique used to measure the time response of accelerator bore pressure, calibration of the instrumentation with nitrogen-pressurization and pyrotechnics, and initial bore pressure measurement attempts. The purpose in presenting this preliminary data is to provide a starting base upon which future researchers may be able to further develop measurement techniques.

Optical sensor technique.—Optical sensors may be used to measure minute displacements. One method is to use parallel bundles of fiber optics as shown in figure 30(a). Half of the bundle transmits light to the sensing end, and the other half serves as receiving elements. Light passes down the transmitting half of the bundle and emerges at the probe end where it reflects from the surface whose displacement is to be measured. The reflected light is picked up by the receiving fibers and carried to a phototransistor which measures light intensity.

When the probe end is touching the surface, no light can be reflected into the receiving fibers, and no output signal is produced. As the probe end is displaced from the surface, light is reflected back into the receiving bundle. The light intensity increases linearly with displacement up to a maximum defined by probe geometry. As displacement increases further, the light intensity decreases in inverse proportion to the square of the displacement. Figure 30(b) shows a typical response curve of the optical sensor. Using the rising portion of the characteristic curve gives better sensitivity but a small working distance. The transmitting and receiving fibers in the bundle may be randomly interspersed for maximum sensitivity.

The use of the optical sensor technique to measure bore pressure allows all electronics to be placed a considerable distance from the rail accelerator and does not require electrically conductive or magnetic materials in the probe and cable.

Experimental setup.—The pressure pulse of the rail accelerator may be transduced by measuring the deflection of the G–10 sidewall material. A 3.18-mm-diameter hole was drilled through the sidewall of the 1-m-long, small-bore (4 by 6 mm), design B rail accelerator to a point within 2 mm of the bore. An aluminum foil reflector was cemented to the bottom of the hole which was carefully finished to be flat and square. As shown in figure 31, a Fotonic probe was then positioned in the hole such that its static operating point was on the rising portion of the response curve (fig. 30(b)). When the rail accelerator is fired, the thin sidewall compresses, and

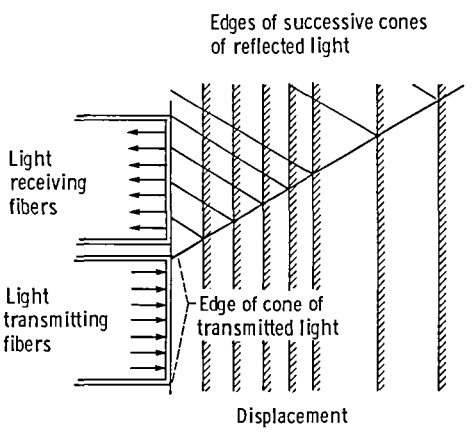

(a) Optical displacement principle.

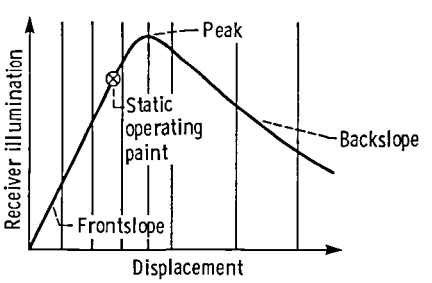

(b) Typical response curve.

Figure 30.—Fiber-optic probe for displacement measurements.

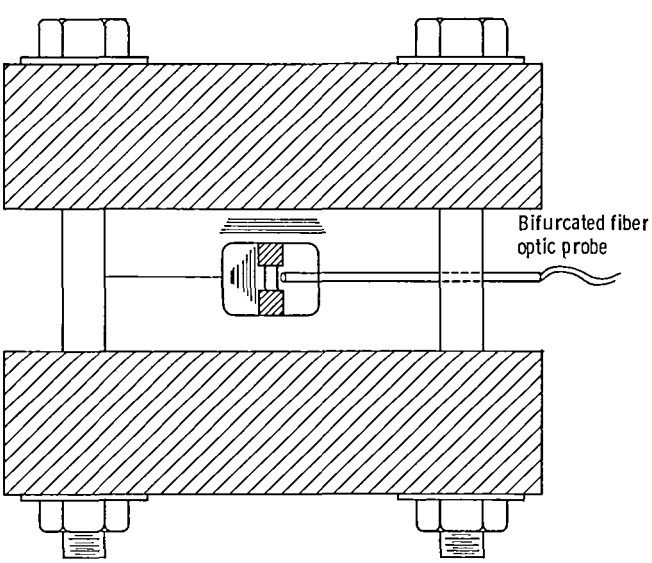

Figure 31.—Fotonic sensor probe installation in 1-m-long, small-bore, design B, rail accelerator. Probe measurement stations are located at 6.4 and 37 cm from breech.

the deflection may be measured by the Fotonic sensor. Bore pressure measurement stations were located at 6.4 and 37.0 cm from the accelerator breech.

Calibration techniques.—Two techniques, nitrogen-pressurization and pyrotechnics, were used to calibrate the Fotonic probes. Both methods relied on pressurizing the rail accelerator bore, measuring the sidewall deflection with the Fotonic sensor, and comparing the probe output with that of a quartz pressure transducer mounted directly opposite the probe station. A Kistler 601 B11 transducer and a Kistler 504 E charge amplifier were used as the calibration standard.

The nitrogen-pressurization technique provided static pressure calibration from 0.7 MPa to 6.9 MPa (100 to 1000 psia). Fixtures were built to plug both the muzzle and the breech ends of the rail accelerator. Nitrogen from a high-pressure bottle was introduced through one end plug. At the maximum pressure level tested (6.9 MPa) the measured deflection was small, and there appeared to be some hysteresis and drift in the measurement.

The pyrotechnic calibration approach provided a short duration pressure pulse to simulate pulsed operating conditions during an actual rail accelerator test. Since the Kistler pressure transducer is rated to approximately 100 MPa (15 000 psi), an attempt was made to generate a bore pressure of this magnitude as a minimum for calibration. (During a rail accelerator test firing, the bore pressure behind the projectile may be as high as 350 MPa.) One end cap of the accelerator was threaded to accept a rifle action chambered for a 300-magnum cartridge. Figure 32 shows the hardware involved. The rifle action is mounted at right angles to the rail accelerator bore so that debris would not blow down the bore and affect the calibration transducer.

Two sets of calibration tests were conducted using Bullseye pistol powder to give a fast rising pulse. Charges ranged from 0.3 g to very nearly a full case (approximately 2.3 g). At the low charge loading, burning was slow and the bore pressure reached less than 13.8 MPa (2000 psi). The high charge loading gave a successful calibration. The produced pressure pulse peaked at 64.8 MPa (9400 psi) and was less than 1 msec wide.

Rail accelerator test firings.—Three tests were made with the Fotonic sensor technique and the small-bore, design B rail accelerator. Figure 33 presents a pressure trace from one of the three tests. The overall shape of the pulse is as expected, but the magnitude indicates some source of error. Based on the static calibration and the zero offset when the probe was installed, the maximum bore pressure that could have been measured was 182 MPa (29 000 psi). The peak pressure of figure 33 is 338 MPa (49 000 psi). A pressure of this magnitude should have driven the system to saturation, even if nonlinearities in the calibration are allowed.

Part of the signal produced was apparently due to noise, even though the sensor electronics were located approximately 3 m from the rail accelerator. A check of the Fotonic sensor system was made by placing an inactive, instrumented rail accelerator

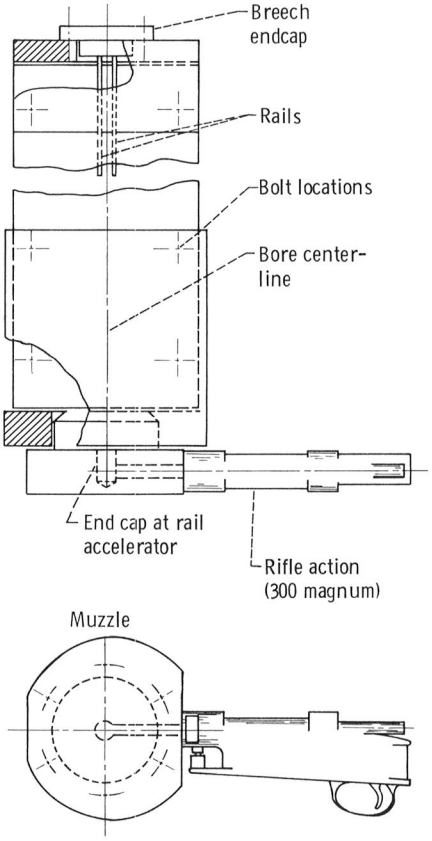

Figure 32.—Top and end views of hardware for pyrotechnic (gun powder) calibration technique. End cap is threaded to accept rifle action at right angles to accelerator bore.

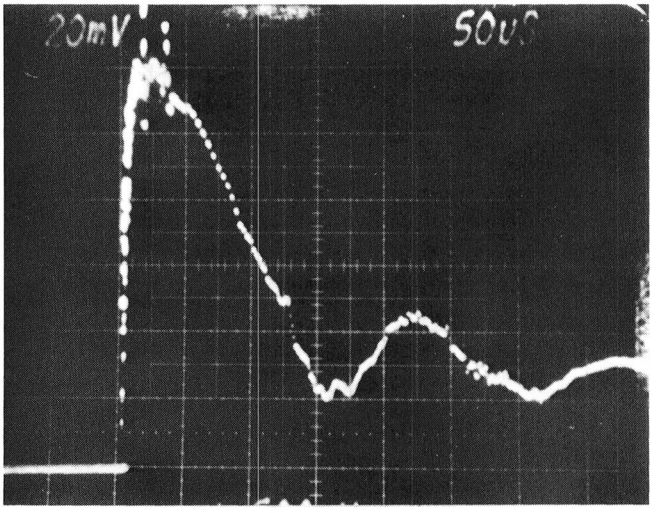

Figure 33.—Pressure pulse with Fontonic sensor instrumentation. Based on static pressure calibration, peak is at 337 MPa (49 000 psi). Probe location, 6.4 cm from breech.

in the vicinity of a noninstrumented rail accelerator being used for a typical test firing. Interference was picked up by Fotonic sensor instrumentation at two intervals. The first noise occurred approximately 20 μsec after the accelerator was fired,

and the second occurred at 135 μsec. This noise accounts for the ragged, leading edge of the pressure trace in figure 33 and the narrow spikes at the peak. Although interference is present in the system during a test firing, it does not account for the large pressure indicated.

One nonelectric problem was identified. The G–10 insulation in the accelerator structure is translucent. Even though the hole surface area was painted black to prevent light from the discharge from getting to the probe, measurements indicated that light from an electronic flash unit could penetrate the G–10 and significantly affect the probe output.

Although the bore pressure measurement techniques described herein were not completely successful, it is thought that the problems encountered are not insurmountable. Recommended improvements to the technique include (1) better shielding of the probe from plasma armature luminosity; (2) operation of the sensor electronics from batteries with more effective electromagnetic shielding; (3) increased strength in the probe to G–10 structure bond; and (4) rigid bonding of the optical fibers to the probe.

Appendix D
Crowbar Ignitron Resistance Measurements

The large single ignitron across each capacitor bank module (fig. 2) serves two purposes. First, it effectively isolates the capacitor banks from the load circuit once the banks have discharged. At this time the current pulse has reached its peak value, and the subsequent decay is then determined primarily by the load inductance and resistance. Second, the use of the crowbar prevents huge voltage reversals in the energy storage capacitors, thereby prolonging capacitor life. Each crowbar ignitron was triggered by a delay generator in the control console at a preset time after the bank was fired. Time delays from 10 μsec to 1.0 msec are available in 10-μsec intervals. In practice, the ignitron can not conduct current until the bank voltage is zero or negative. The crowbar ignitrons used with the capacitor bank modules (General Electric GL820J-M) are rated by the manufacturer at a maximum peak current of 600 kA and a charge transfer of 1500 C. The resistance of the crowbar ignitron while in the conduction state has been estimated at less than 10 mΩ (ref. 27).

The resistance of the crowbar is significant because the rail accelerator current flows through the crowbar. Any I^2R losses in the ignitron, then, detract from the energy available for acceleration. Crowbar losses become insignificant if sufficient energy stores are available. However, most rail accelerator designs and test firings are limited in velocity and/or projectile mass by the size of the available energy storage. Therefore, it is important to both minimize crowbar resistance and to quantify that resistance as a function of crowbar current, in order to predict and obtain maximum projectile velocity and mass for a given rail accelerator test firing. For example, a crowbar with a 2-mΩ resistance would waste twice as much energy as that which is consumed by a typical plasma armature.

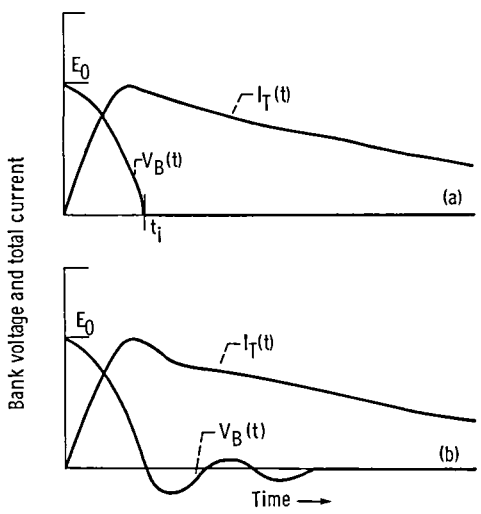

(a) Ideal discharge. For $t<t_1$, $R<2\ L/C$; for $t>t_1$, $C=0$.
(b) Actual discharge due to stray reactive components.

Figure 34.—Pulsed power operation with crowbar ignitron.

Figure 34(a) illustrates the ideal mode of pulsed power operation with the crowbar ignition as shown in the electrical schematic of figure 2. When the bank is fired, the characteristics of the resultant current pulse are determined by the constant capacitance and time-varying inductance and resistance of the circuit. (These latter parameters change due to the variable electrical characteristics of the rail accelerator.) As the capacitor bank voltage nears zero, the current has already begun to decay from its peak value. The crowbar is fired when the bank voltage becomes zero. The unidirectional current flowing through the crowbar ignitron and the load may be described as,

$$I_L(t)=I_c e^{-(R/L)t} \tag{D1}$$

where

I_L instantaneous load current, A
I_c the current at time of crowbar, A
R total circuit resistance, Ω
L total circuit inductance, H
t time, sec

Stray inductive components in the capacitor bank side of the schematic (fig. 2) cause oscillations in the bank voltage as described in figure 34(b). Consequently, the current in the rail accelerator load reflects these oscillations. In this case the actual current flowing in crowbar ignitron is equal to the load current minus the oscillatory current trapped in the bank circuit.

A crowbar ignitron does not necessarily have constant resistance with increasing energy. Very little data are given in the literature (ref. 28), particularly for currents above 50 kA. Measurements of the crowbar voltage during rail accelerator test firings were made with the goal of quantifying the crowbar ignitron resistance up to currents of 200 kA and to gain a better understanding of the actual capacitor bank discharge. The measurements were made with a 1.0-kΩ divider network consisting of low inductance carbon resistors used in combination with a small current transformer (Pearson 4100: output, 1 V/A).

Figure 35 plots crowbar voltage as a function of load current. The data were taken at a point where the stray bank current oscillations have died out; therefore, it can be assumed that the crowbar current equals the load current. The data points in figure 35(a) are from test firings with one capacitor

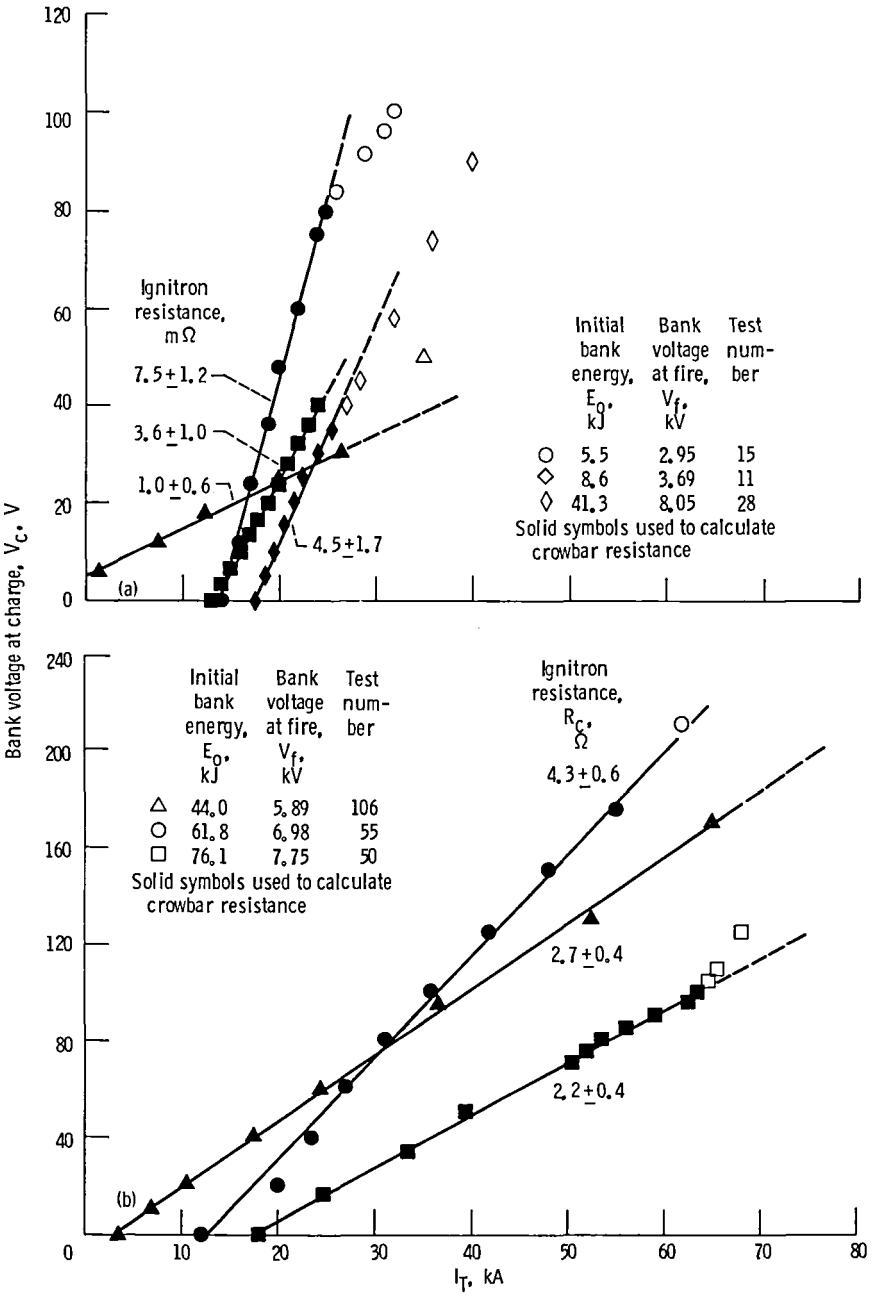

(a) One module at various energy levels.
(b) Two modules at various energy levels.

Figure 35.—Voltage-current characteristics of crowbar ignitron.

bank module (one crowbar ignitron) at varying initial energy levels. Crowbar resistance varies from 1.0 ± 0.6 to 7.5 ± 1.2 mΩ. The voltage versus current characteristics appear to be linear up to approximately 25 kA, at which point substantial deviations occur. The data points in figure 35(b) are taken from test firings using two modules (and, therefore, two crowbar ignitrons in parallel). Calculation of resistance is based on the assumption that the current divides evenly between the two ignitrons. Here, ignitron resistance appears to be approximately 2.2 ± 0.4 to 4.3 ± 0.6 mΩ and voltage-current data is linear up to approximately 60 kA.

References

1. Rashleigh, S.C.; and Marshall, R.A.: Electromagnetic Acceleration of Macroparticles to High Velocities. J. Appl. Phys., vol. 49, no. 4, Apr. 1978, pp. 2540-2542.
2. Barber, J.P.: The Acceleration of Macroparticles and a Hypervelocity Electromagnetic Accelerator. Australian National University, Department of Engineering Physics, EP-T12, 1972.
3. Bauer, D.P.; and Barber, J.P.: Application of an Electric Rail Gun to Space Propulsion. AIAA Paper No. 81-0704, Apr. 1981.
4. Rice, E.E.; Miller, L.A.; and Earhart, R.W.: Preliminary Feasibility Assessment for Earth-to-Space Electromagnetic (Railgun) Launchers. NASA CR-167886, 1982.
5. Miller, L.A., et al.: Preliminary Analysis of Space Mission Applications for Electromagnetic Launchers. NASA CR-174067, 1984
6. Zana, L.M., et al.: NASA Lewis Rail Accelerators: Test Designs and Diagnostic Techniques. IEEE Trans. Magn., vol. 20, no. 2, Mar. 1984, pp. 324-327.
7. Bauer, D.P.; McCormick, T.J.; and Barber, J.P.: Electric Rail Gun Projectile Acceleration to High Velocity. AIAA Paper No. 82-1939, Nov. 1982.
8. Bauer, D.P.; McCormick, T.J.; and Barber, J.P.: Electric Rail Launcher System Design and Test Evaluation. IAP Research, Inc., Dayton, OH, IAP-TR-82-6, Nov. 1982.
9. Kerslake, W.R.; and Cybyk, B.Z.: Rail Accelerator Research at Lewis Research Center. AIAA Paper 82-1938 (See also NASA TM-83015), Nov. 1981.
10. Grover, F.W.: Inductance Calculations. D. Van Nostrand Co., Inc. New York, 1946.
11. Kerrisk, J.F.: Current Distribution and Inductance Calculations for Rail-Gun Conductors. Los Alamos National Laboratory, LA-9092-MS, 1981.
12. Kerrisk, J.F.: Current Diffusion in Railgun Conductors. Los Alamos National Laboratory, LA-9401-MS, June 1982.
13. McNab, I.R.: Electromagnetic Macroparticle Acceleration by a High Pressure Plasma. J. Appl. Phys., vol. 51, no. 5, May 1980, pp. 2549-2551.
14. Powell, J.D.; and Batteh, J.H.: Plasma Dynamics of an Arc-Driven, Electromagnetic, Projectile Accelerator. J. Appl. Phys., vol. 52, no. 4, Apr. 1981, pp. 2717-2730.
15. Powell, J.D.: Two Dimensional Model for Arc Dynamics in the Rail Gun. Army Armament Research and Development Command, Aberdeen Proving Ground, MD, Ballistic Research Lab., ARBRL-TR-02423, Oct. 1982. (AD-A120046)
16. Thio, Y.C.: PARA: A Computer Simulation Code for Plasma Driven Electromagnetic Launchers. Materials Research Labs, Melbourne, Australia, MRL-R-873, Mar. 1983.
17. Ray,Pradash K.: Arc-Driven Rail Gun Research. NASA CR-174816, 1984.
18. Gooder, S.T.: Electromagnetic Propulsion Test Facility. NASA TM-83568, 1984.
19. Jamison, K.A.; and Burden, H.S.: Arc Armature Diagnostics Experiments on an Electromagnetic Gun. ARRADCOM Technical Conference, July 1982.
20. Stainsby, D.F.; and Bedford, A.J.: Some Diagnostic Interpretations from Railgun Plasma Profile Experiments. IEEE Trans. Magn., vol. 20, no. 2, Mar. 1984, pp. 332-335.
21. Parker, J.V.; and Parsons, W.M.: Effect of Ablation on Plasma Armature Dynamics. Presented at DARPA/Service Electromagnetic Propulsion Program Review, Arlington, VA, Sept. 18-20, 1984.
22. Parker, J.V., et al.: Plasma Armature Railgun Studies. Presented at the IEEE Conference on Plasma Science, Pittsburgh, PA, June 1985.
23. Wang, S.Y.: Structural Response of a Rail Accelerator. IEEE Trans. Magn., vol. 20, no. 2, Mar. 1984, pp. 356-359.
24. Bedford, A.J.: Rail Damage in a Small Calibre Railgun. IEEE Trans. Magn., vol. 20, no. 2, Mar. 1984, pp. 348-351.
25. Bedford, A.J.: Plasma Mass and Effective Inductance in a Small Railgun. Aeronautical Research Labs, Melbourne, Australia, MRL-R-947, AR-004-195, Nov. 1984.
26. Powell, J.D.: Effects of Atmospheric Air on Projectile Acceleration in the Railgun. Army Armament Research and Development Center, Aberdeen Proving Ground, MD, Ballistic Research Lab., ARBRL-MR-03332, Feb. 1984. (AD-A138790)
27. Ignitrons in Capacitor Discharge and Crowbar Service. General Electric Tube Products Dept., Schenectady, NY, PT-57B, Aug. 19-78, p. 15.

1. Report No.	2. Government Accession No.	3. Recipient's Catalog No.
NASA TP-2571		

4. Title and Subtitle	5. Report Date
Rail Accelerators for Space Transportation - An Experimental Investigation	May 1986
	6. Performing Organization Code: 506-55-22

7. Author(s)	8. Performing Organization Report No.
Lynnette M. Zana, William R. Kerslake, and John L. Sturman	E-2754
	10. Work Unit No.

9. Performing Organization Name and Address	11. Contract or Grant No.
National Aeronautics and Space Administration Lewis Research Center Cleveland, Ohio 44135	
	13. Type of Report and Period Covered: Technical Paper

12. Sponsoring Agency Name and Address	14. Sponsoring Agency Code
National Aeronautics and Space Administration Washington, D.C. 20546	

15. *Supplementary Notes*

16. Abstract

An experimental program was conducted at the Lewis Research Center with the objective of investigating the technical feasibility of rail accelerators for propulsion applications. Single-stage, plasma driven rail accelerators of small (4 by 6 mm) and medium (12.5 by 12.5 mm) bores were tested at peak accelerating currents of 50 to 450 kA. Streak-camera photography was used to provide a qualitative description of plasma armature acceleration. The effects of plasma blowby and varying bore pressure on the behavior of plasma armatures were studied.

17. Key Words (Suggested by Author(s))	18. Distribution Statement
Electromagnetic launchers; Rail accelerators; Railguns	Unclassified - unlimited STAR Category 20

19. Security Classif. (of this report)	20. Security Classif. (of this page)	21. No. of pages	22. Price*
Unclassified	Unclassified	36	A03

*For sale by the National Technical Information Service, Springfield, Virginia 22161

NASA-Langley, 1986

National Aeronautics and
Space Administration
Code NIT-4

Washington, D.C.
20546-0001

BULK RATE
POSTAGE & FEES PAID
NASA
Permit No. G-27